Pseudogap temperature T^* of cuprate superconductors from the Nernst effect

O. Cyr-Choinière,[1,*] R. Daou,[1,†] F. Laliberté,[1] C. Collignon,[1] S. Badoux,[1] D. LeBoeuf,[1,‡] J. Chang,[1,§] B. J. Ramshaw,[2,∥] D. A. Bonn,[2,3] W. N. Hardy,[2,3] R. Liang,[2,3] J.-Q. Yan,[4] J.-G. Cheng,[5] J.-S. Zhou,[5] J. B. Goodenough,[5] S. Pyon,[6] T. Takayama,[6] H. Takagi,[6,7,¶] N. Doiron-Leyraud,[1] and Louis Taillefer[1,3,#]

[1] *Institut quantique, Département de physique & RQMP, Université de Sherbrooke, Sherbrooke, Québec J1K 2R1, Canada*
[2] *Department of Physics and Astronomy, University of British Columbia, Vancouver, British Columbia V6T 1Z4, Canada*
[3] *Canadian Institute for Advanced Research, Toronto, Ontario M5G 1Z8, Canada*
[4] *Ames Laboratory, Ames, Iowa 50011, USA*
[5] *University of Texas - Austin, Austin, Texas 78712, USA*
[6] *Department of Advanced Materials, University of Tokyo, Kashiwa 277-8561, Japan*
[7] *RIKEN (The Institute of Physical and Chemical Research), Wako 351-0198, Japan*

(Received 22 March 2017; revised manuscript received 26 December 2017; published 1 February 2018)

We use the Nernst effect to delineate the boundary of the pseudogap phase in the temperature-doping phase diagram of hole-doped cuprate superconductors. New data for the Nernst coefficient $\nu(T)$ of $YBa_2Cu_3O_y$ (YBCO), $La_{1.8-x}Eu_{0.2}Sr_xCuO_4$ (Eu-LSCO), and $La_{1.6-x}Nd_{0.4}Sr_xCuO_4$ (Nd-LSCO) are presented and compared with previously published data on YBCO, Eu-LSCO, Nd-LSCO, and $La_{2-x}Sr_xCuO_4$ (LSCO). The temperature T_ν at which ν/T deviates from its high-temperature linear behavior is found to coincide with the temperature at which the resistivity $\rho(T)$ deviates from its linear-T dependence, which we take as the definition of the pseudogap temperature $T^\star$—in agreement with the temperature at which the antinodal spectral gap detected in angle-resolved photoemission spectroscopy (ARPES) opens. We track $T^\star$ as a function of doping and find that it decreases linearly vs p in all four materials, having the same value in the three LSCO-based cuprates, irrespective of their different crystal structures. At low p, $T^\star$ is higher than the onset temperature of the various orders observed in underdoped cuprates, suggesting that these orders are secondary instabilities of the pseudogap phase. A linear extrapolation of $T^\star(p)$ to $p = 0$ yields $T^\star(p \to 0) \simeq T_N(0)$, the Néel temperature for the onset of antiferromagnetic order at $p = 0$, suggesting that there is a link between pseudogap and antiferromagnetism. With increasing p, $T^\star(p)$ extrapolates linearly to zero at $p \simeq p_{c2}$, the critical doping below which superconductivity emerges at high doping, suggesting that the conditions which favor pseudogap formation also favor pairing. We also use the Nernst effect to investigate how far superconducting fluctuations extend above the critical temperature T_c, as a function of doping, and find that a narrow fluctuation regime tracks T_c, and not $T^\star$. This confirms that the pseudogap phase is not a form of precursor superconductivity, and fluctuations in the phase of the superconducting order parameter are not what causes T_c to fall on the underdoped side of the T_c dome.

DOI: 10.1103/PhysRevB.97.064502

I. INTRODUCTION

Understanding the mechanisms responsible for superconductivity in cuprates requires that we elucidate the nature of the enigmatic pseudogap phase that coexists with the superconducting phase in their temperature-doping phase diagram. The pseudogap is a partial gap in the spectral function that opens at the Fermi energy in k-space locations $(\pm\pi,0)$ and $(0,\pm\pi)$, the so-called antinodal regions of the first Brillouin zone, as measured by angle-resolved photoemission spectroscopy (ARPES) [1]. It is essential to know the boundary of the pseudogap phase, i.e., the location of the pseudogap temperature $T^\star$ as a function of doping p and of the critical doping $p^\star$ where the pseudogap phase ends at $T = 0$.

Nd-LSCO is the only cuprate material for which this information is complete. Here, the critical point has been located at $p^\star = 0.23 \pm 0.01$, from in-plane resistivity [2,3], out-of-plane resistivity [4], and Hall effect [3]. This location is consistent with ARPES measurements at low temperature that find a large pseudogap at $p = 0.20$ but none at $p = 0.24$ [5]. Moreover, in Nd-LSCO the temperature T_ρ below which the resistivity $\rho(T)$ deviates from its linear-T dependence at high T [2,3] agrees with the onset temperature for the opening of the pseudogap measured by ARPES [5]. This shows that resistivity measurements can be used to track $T^\star = T_\rho$ vs p in Nd-LSCO.

In only two other cuprates is the location of $p^\star$ well established. In YBCO, recent high-field Hall measurements in the $T = 0$ limit find $p^\star = 0.195 \pm 0.005$ [6], in agreement

*Present address: Yale School of Engineering and Applied Science, Yale University, New Haven, Connecticut 06511, USA.
†Present address: Laboratoire CRISMAT, CNRS, Caen, France.
‡Present address: Laboratoire National des Champs Magnétiques Intenses, UPR 3228, (CNRS-INSA-UJF-UPS), Grenoble 38042, France.
§Present address: Department of Physics, University of Zurich, Winterthurerstrasse 190, 8057 Zurich, Switzerland.
∥Present address: Department of Physics, Cornell University, 531 Clark Hall, Ithaca, NY, 14853-2501, USA.
¶Present address: Max Planck Institute for Solid State Research, 70569 Stuttgart, Germany.
#louis.taillefer@usherbrooke.ca

with earlier analyses that yield $p^\star = 0.19 \pm 0.01$ [7]. However, there are no ARPES measurements of $T^\star$ in YBCO, so one typically relies on T_ρ determined from resistivity without spectroscopic confirmation, and there is some debate as to where T_ρ crosses the superconducting temperature T_c [8]. In LSCO, high-field resistivity measurements in the $T = 0$ limit [9–11] yield $p^\star = 0.18 \pm 0.01$ [11]. However, there is no consensus on the location of the $T^\star(p)$ line in the phase diagram of LSCO [12,13].

In $Bi_2Sr_{2-x}La_xCuO_{6+\delta}$ (Bi-2201) [14] and $Bi_2Sr_2CaCu_2O_{8+\delta}$ (Bi-2212) [15], ARPES measurements have delineated the $T^\star(p)$ line quite well, and it is found to agree with T_ρ from resistivity. However, there is no agreement on the location of $p^\star$. In Bi-2201, STM measurements suggest that $p^\star > p_{c2}$, the critical doping below which superconductivity emerges at high doping [16], while NMR measurements show that $p^\star < p_{c2}$ [17]. In Bi-2212, STM measurements find that $p^\star = 0.19$ (in the superconducting state) [18], while Raman measurements find $p^\star = 0.22$ (in the normal state) [19].

In this paper, we show that the Nernst effect can be used to detect $T^\star$, not only in YBCO and $HgBa_2CuO_{4+\delta}$ (Hg-1201), as shown previously [20,21], but also in the LSCO-based cuprates. We present data on YBCO, Nd-LSCO, and Eu-LSCO, and combine these with published data on LSCO, Nd-LSCO, and Eu-LSCO, to determine the pseudogap boundary in all four materials. We find that the three LSCO-based cuprates have the same $T^\star(p)$ line up to $p \simeq 0.17$, irrespective of their different crystal structures. This suggests that the interactions responsible for the pseudogap have the same strength. From the fact that $p^\star$ is quite different in LSCO and Nd-LSCO (0.18 vs 0.23), we infer that additional mechanisms must dictate the location of the $T = 0$ critical point [22]. $T^\star$ lies on a line that connects T_N at $p = 0$, the Néel temperature for antiferromagnetic order at zero doping, to p_{c2}. In YBCO, we again find that $T^\star$ lies on a line connecting T_N and p_{c2}, even if T_N is now a factor 1.5 larger. In other words, $T^\star$ in YBCO is 1.5 times larger than in LSCO. This suggests a link between antiferromagnetism, pseudogap, and superconductivity.

The paper is organized as follows. In Sec. II, we give a brief introduction to the Nernst effect. In Sec. III, we provide information on the experimental measurement of the Nernst effect. In Sec. IV, we establish the $T^\star(p)$ line for YBCO. In Sec. V, we establish the $T^\star(p)$ line for LSCO, Nd-LSCO, and Eu-LSCO. We show in detail how $T^\star$ is independent of crystal structure. In the discussion (Sec. VI), we compare YBCO and LSCO, and draw general observations about the pseudogap phase. We also plot the onset temperatures of various orders on the phase diagrams of YBCO and LSCO and discuss the implications. In the Appendix, we show how superconducting fluctuations in YBCO, LSCO, Hg-1201, Bi-2212, and Bi-2201 are limited to a region close to T_c, well below $T^\star(p)$, and explain why previous interpretations suggested a much wider regime of fluctuations.

II. THE NERNST EFFECT

The Nernst effect is the development of a transverse electric field E_y across the width (y axis) of a metallic sample when a temperature gradient $\partial T/\partial x$ is applied along its length (x axis) in the presence of a perpendicular magnetic field H (along the z axis). Two mechanisms can give rise to a Nernst signal $N \equiv E_y/(-\partial T/\partial x)$ [23–25]: superconducting fluctuations [26–28], which give a positive signal, and charge carriers (quasiparticles), which can give a signal of either sign. The focus of this paper is on the quasiparticle contribution to the Nernst effect in cuprates.

In the Appendix, we discuss the contribution of superconducting fluctuations to the Nernst signal in cuprates and explain how the traditional assumption that it is the only significant contribution is mistaken. We discriminate between the superconducting signal and the quasiparticle signal by using the fact that only the former is suppressed by a magnetic field. We show that the regime of significant superconducting fluctuations is a relatively narrow band that tracks T_c, completely distinct from $T^\star$. This confirms that the pseudogap phase is not caused by fluctuations in the phase and/or the amplitude of the superconducting order parameter.

The Nernst signal is related to the conductivity $\overleftrightarrow{\sigma}$ and thermoelectric $\overleftrightarrow{\alpha}$ tensors via

$$N = \frac{\alpha_{xy}\sigma_{xx} - \alpha_{xx}\sigma_{xy}}{\sigma_{xx}^2 + \sigma_{xy}^2} \simeq \frac{\alpha_{xy}}{\sigma_{xx}} - S\frac{\sigma_{xy}}{\sigma_{xx}}, \tag{1}$$

where $S \equiv \alpha_{xx}/\sigma_{xx}$ is the Seebeck coefficient. In-plane isotropy is assumed ($\sigma_{xx} = \sigma_{yy}$) and the approximate expression on the right holds for $\sigma_{xx}^2 \gg \sigma_{xy}^2$.

The sign of N will thus depend on the relative magnitude of $\alpha_{xy}\sigma_{xx}$ and $\alpha_{xx}\sigma_{xy}$. In a single-band metal with an energy-independent Hall angle θ_H, where $\tan\theta_H \equiv \sigma_{xy}/\sigma_{xx}$, the two terms are equal and thus $N = 0$ [23–25]. This is the so-called Sondheimer cancellation. An energy dependence of θ_H will offset this equality in a direction that is difficult to predict, resulting in a finite N whose sign can be either positive or negative [23–25]. In general, the sign of N in metals is not understood. Even in single-band metals like overdoped cuprates, it is unclear why $N > 0$ in the electron-doped material $Pr_{2-x}Ce_xCuO_4$ (PCCO) [29] and $N < 0$ in the hole-doped material Nd-LSCO [30], since both have a positive Hall coefficient.

At low temperature, the magnitude of the quasiparticle Nernst signal is given approximately by [23–25]:

$$\frac{|\nu|}{T} \approx \frac{\pi^2}{3}\frac{k_B^2}{e}\frac{\mu}{\epsilon_F}, \tag{2}$$

where $\nu \equiv N/H$ is the Nernst coefficient, H is the magnetic field, T is the temperature, k_B is Boltzmann's constant, e is the electron charge, μ is the carrier mobility, and ϵ_F is the Fermi energy. Equation (2) works remarkably well as a universal expression for the Nernst coefficient of metals at $T \to 0$, accurate within a factor two or so in a wide range of materials [23]. It explains why a phase transition that reconstructs a large Fermi surface into small pockets (with small ϵ_F) can cause a major enhancement of ν. The heavy-fermion metal URu_2Si_2 provides a good example of this. As the temperature drops below its transition to a metallic state with reconstructed Fermi surface at 17 K, the carrier density n (or ϵ_F) falls and the mobility rises, both by roughly a factor 10, and ν/T increases by a factor 100 or so [31]. Note that the electrical resistivity $\rho(T)$ is affected only weakly by these dramatic changes [32], since mobility and carrier density are modified in ways that compensate in the conductivity $\sigma = 1/\rho = ne\mu$.

This is why the Nernst effect can be a more sensitive probe of electronic transformations, such as density-wave transitions, than the resistivity. Here we use it to study the pseudogap phase of cuprate superconductors.

III. METHODS

The YBCO samples measured here ($p = 0.078$ and $p = 0.085$) were single crystals prepared at the University of British Columbia by flux growth [33]. The detwinned samples are uncut, unpolished thin platelets, with gold evaporated contacts (of resistance <1 Ω), in a six-contact geometry. Typical sample dimensions are 20–50 × 500–800 × 500–1000 μm^3 (thickness × width × length). Their hole concentration (doping) p was determined from a relationship between the c-axis lattice constant and the superconducting transition temperature T_c [34], defined as the temperature below which the zero-field resistance is zero.

The Nd-LSCO samples ($x = 0.20$ and 0.21) and the Eu-LSCO samples ($x = 0.08$, 0.10, and 0.21) measured here were grown using a traveling float-zone technique in an image furnace at the University of Texas and the University of Tokyo, respectively. ab-plane single crystals were cut from boules into small rectangular platelets with typical dimensions of 1 mm in length and 0.5 mm in width (in the basal plane of the tetragonal structure), with a thickness of 0.2 mm along the c axis. Orientation was checked via Laue diffraction. The doping p is taken to equal the Sr content x, to within ±0.005. The T_c of our samples was determined via resistivity measurements as the temperature where $\rho(T)$ goes to zero. Electrical contacts on the Nd/Eu-LSCO samples were made to the crystal surface using Epo-Tek H20E silver epoxy, cured at 180 °C for 5 min and then annealed at 500 °C in flowing oxygen for 1 hr. This resulted in contact resistances of less than 1 Ω at room temperature. The longitudinal contacts were wrapped around all four sides of the sample. The current contacts covered the end faces. Nernst (transverse) contacts were placed opposite to each other in the middle of the sample, extending along the length of the c axis, on the sides. The uncertainty in the length L of the sample (between longitudinal contacts) reflects the width of the voltage/temperature contacts along the x axis.

Figure 1 summarizes how the Nernst signal is measured. The Nernst signal was measured by applying a steady heat current through the sample (along the x axis). The longitudinal thermal gradient was measured using two uncalibrated Cernox chip thermometers (Lakeshore), referenced to a further calibrated Cernox. Alternatively on some samples, the longitudinal thermal gradient was measured using one differential and one absolute type-E thermocouple made of chromel and constantan wires known to have a weak magnetic field dependence. The temperature of the experiment was stabilized at each point to within ±10 mK. The temperature and voltage were measured with and without applied thermal gradient (ΔT) for calibration. The magnetic field H, applied along the c axis ($H \parallel c$), was then swept with the heat on, from $-H_{max}$ to $+H_{max}$ (where $H_{max} = 10$, 15, or 16 T depending on sample), at 0.4 T/min, continuously taking data. The thermal gradient was monitored continuously and remained constant during the course of a sweep. The Nernst signal N was extracted from that part of the measured voltage which is antisymmetric with respect to

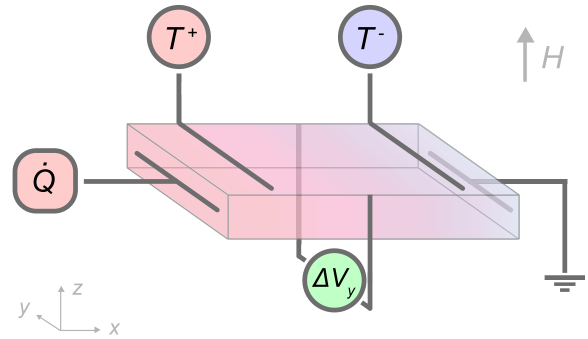

FIG. 1. Sketch of how the Nernst effect is measured on a sample in the shape of a thin platelet. A longitudinal temperature gradient along x is generated by applying heat to one end of the sample, while the other end is kept cold. A given heat current ($\dot{Q}$) produces a temperature difference ($\Delta T_x = T^+ - T^-$) that can be measured either with resistance thermometers or thermocouples. When a magnetic field (H) is applied along z, a transverse (Nernst) voltage (ΔV_y) is generated. The Nernst signal N is the ratio of ΔV_y over ΔT_x [Eq. (3)].

the magnetic field:

$$N = \frac{E_y}{\partial T/\partial x} = \left(\frac{\Delta V_y(+H)}{\Delta T_x} - \frac{\Delta V_y(-H)}{\Delta T_x}\right)\frac{L}{2w}, \quad (3)$$

where ΔV_y is the difference in the voltage measured with and without thermal gradient. L is the length (between contacts along the x axis) and w the width (along the y axis) of the sample. This antisymmetrization procedure removes any longitudinal thermoelectric contribution from the sample and a constant background from the measurement circuit. The uncertainty on N comes mostly from the uncertainty in measuring L and w, giving a typical error bar of ±10% on N.

IV. YBCO

Nernst data taken on untwinned single crystals of YBCO have been reported for a range of dopings, from $p = 0.11$ to $p = 0.18$ [20]. A typical set of Nernst data is reproduced in Fig. 2 as ν/T vs T, for a sample with $p = 0.12$. Two separate contributions are clearly seen: 1) a positive and magnetic-field-dependent signal which rises below a temperature T_{min} close to T_c; 2) a field-independent signal which goes from small and positive at high temperature to large and negative at lower temperature, as it drops below a temperature T_ν. The first is due to superconducting fluctuations, the second is due to quasiparticles. In Fig. 3, the two onset temperatures T_{min} and T_ν are plotted on a phase diagram. The 10 data points for T_ν (red squares) at $p > 0.1$ are reproduced from Ref. [20]; they include data taken with $\Delta T || a$ and $\Delta T || b$—both yield the same T_ν [20]. In Fig. 4, we report data for dopings $p = 0.078$ and $p = 0.085$ which allow us to extend T_ν to low doping.

In YBCO, a standard criterion for the pseudogap temperature $T^\star$ is the temperature T_ρ below which the a-axis resistivity $\rho(T)$ deviates from its linear temperature dependence at high temperature [36]. An example is shown in Fig. 5(a), where we extract $T_\rho = 200 \pm 10$ K from published data at $p = 0.13$ [12]. Values for T_ρ at different dopings are plotted on the phase diagram of Fig. 3, where we see that $T_\nu = T_\rho$, within error bars.

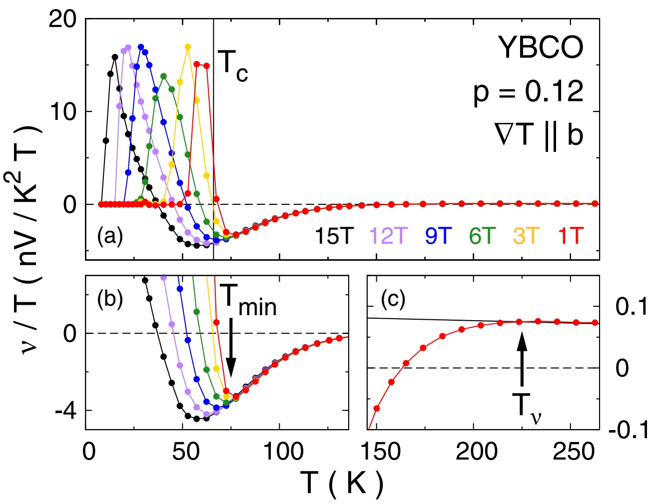

FIG. 2. Nernst coefficient ν of YBCO at a hole doping of $p = 0.12$, plotted as ν/T versus temperature T for different magnetic fields ($H = 1$ T to 15 T), as indicated. The thermal gradient is applied in the b direction of the orthorhombic crystal structure. Data are reproduced from Ref. [20]. (a) The vertical line marks the superconducting transition temperature at $H = 0$, $T_c = 66.0$ K. (b) Zoom near T_c, to show how T_{min} is defined: It is the temperature at which the Nernst signal at $H = 1$ T goes through a minimum, at the foot of the large positive peak due to superconductivity. (c) Zoom at high temperature, where only quasiparticles contribute to the Nernst signal. T_ν (arrow) is defined as the temperature below which $\nu(T)/T$ starts to deviate downwards from its high-temperature linear behavior.

As a probe of the pseudogap phase in YBCO, the Nernst effect has an advantage over the resistivity. Pseudogap and superconductivity have opposite effects on $\nu(T)$: the former causes it to fall to negative values upon cooling, the latter causes it to rise, while for resistivity, both phenomena yield a downturn in $\rho(T)$ [see Fig. 5(a), Fig. 6, and the paragraph below]. This makes the separation of the two contributions in the Nernst effect unambiguous, and allows us to track their respective onset temperatures.

In Fig. 6, we plot T_ν and T_{min} on the "curvature map" produced by Ando and Segawa [12] from the second temperature derivative of their $\rho(T)$ data. As already seen in Fig. 3, the lower bound of the linear-T region (white region in the upper right corner of Fig. 6) coincides with T_ν and defines the boundary of the pseudogap phase. Below $T^\star$, the initial drop in $\rho(T)$ shows up as a blue band, followed by an upturn (in red) (for $p < 0.13$, in Fig. 6). Superconducting fluctuations above T_c also cause a downturn in $\rho(T)$ (called "paraconductivity"), producing another blue band, which simply tracks T_c. For $p < 0.13$, the onset of paraconductivity coincides reasonably well with T_{min}. Therefore T_{min} is the temperature below which superconducting fluctuations (above T_c) start to show up significantly in the Nernst signal. For $p > 0.13$, the two blue bands merge and become indistinguishable—the pseudogap downturn flows smoothly into the paraconductivity downturn (see Fig. 6). This makes it difficult to reliably track $T^\star$ above $p = 0.13$, and to say from the resistivity whether there is still a pseudogap phase (with $T^\star > T_c$) beyond optimal doping. From the Nernst data, however, the answer is clearly yes, with $T^\star \simeq 140$ K and $T_c = 90$ K at $p = 0.18$.

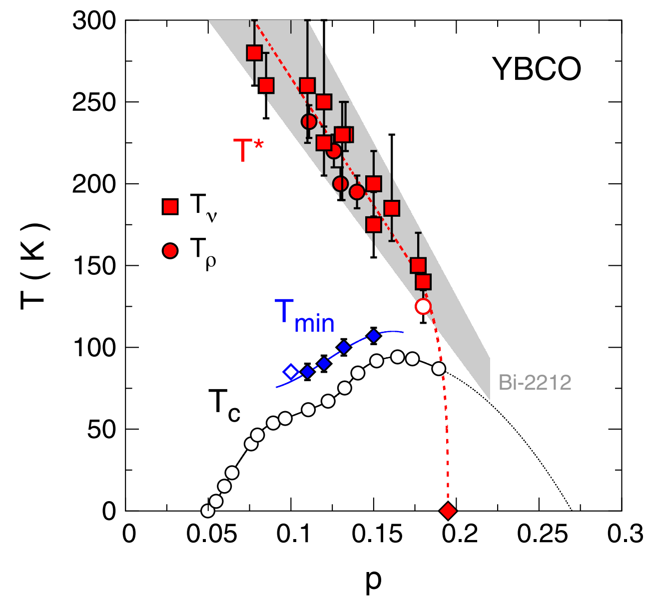

FIG. 3. Temperature-doping phase diagram of YBCO, showing three characteristic temperatures. The transition temperature T_c (open black circles [34]) marks the onset of superconductivity in zero magnetic field, below which the electrical resistivity is zero. The solid black line is a guide to the eye through the T_c data points. The dotted black line is a smooth extension of this line assuming that the superconducting phase ends at a critical doping $p_{c2} = 0.27$. Blue diamonds mark T_{min} [defined in Fig. 2(b)], the temperature below which superconducting fluctuations become significant (from a-axis data in Ref. [20]). The open diamond shows T_{min} for a previously measured sample with $p = 0.1$ [35]. The solid blue line is a guide to the eye. Red circles mark T_ρ, the temperature below which the resistivity $\rho(T)$ deviates from its high-temperature linear dependence (from data in Ref. [12]), a standard definition of the pseudogap temperature $T^\star$ in YBCO [36] [see Fig. 5(a)]. The open red circle shows T_ρ for a sample with $p = 0.18$ in which a high level of disorder scattering was introduced by electron irradiation [37]. In this case, T_ρ marks the onset of an upturn in $\rho(T)$ (see text). Red squares mark T_ν [defined in Fig. 2(c)], the temperature below which the quasiparticle Nernst signal departs from its high-temperature behavior (from present work and Ref. [20]). One can see that within error bars, $T_\nu \simeq T_\rho$, both measures of $T^\star$. The red dashed line is a linear fit through the $T^\star$ data points. Beyond $p = 0.18$, it is a guide to the eye extending smoothly to reach $p = p^\star$ at $T = 0$ (red diamond). $p^\star$ is the critical doping where the pseudogap phase ends at $T = 0$ in the absence of superconductivity. In YBCO, $p^\star = 0.195 \pm 0.005$ [6]. The gray band marks the range of $T^\star$ values measured in Bi-2212 from spectroscopic probes (ARPES, STS, and SIS) [15], detected up to $p \simeq 0.22$.

While in YBCO the signature of $T^\star$ is a downturn in both $\rho(T)$ and ν/T, we shall see below that the corresponding signature in LSCO is an upturn in those two quantities (see Figs. 5 and 7). We attribute this difference to a difference in the relative importance of two effects of the pseudogap: the loss of carrier density and the loss of inelastic scattering. At $T = 0$, there is no inelastic scattering and so only the first effect is relevant. It has recently become clear that in the normal state at $T = 0$ the opening of the pseudogap at $p = p^\star$ causes a rapid drop in the carrier density n from $n = 1 + p$

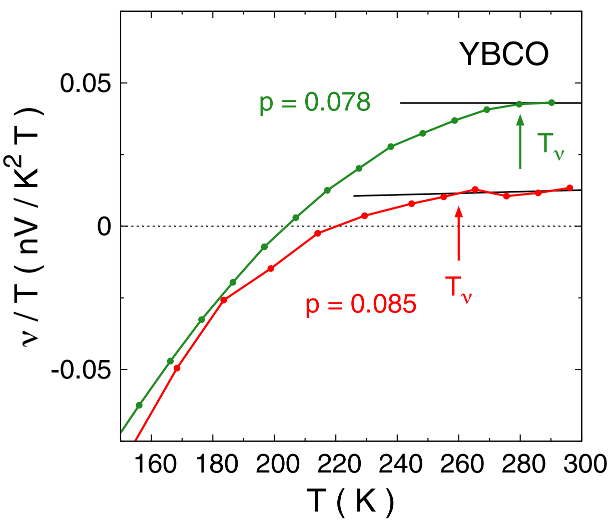

FIG. 4. High-temperature Nernst coefficient ν of YBCO at dopings $p = 0.078$ (green) and $p = 0.085$ (red), plotted as ν/T versus T. The thermal gradient was applied in the a direction. The color-coded arrows mark T_ν, the temperature below which $\nu(T)/T$ starts to deviate downwards from its small, roughly constant value at high temperature: $T_\nu = 280 \pm 20$ K and 260 ± 20 K for $p = 0.078$ and 0.085, respectively. Error bars on T_ν represent the uncertainty in identifying the start of the downturn.

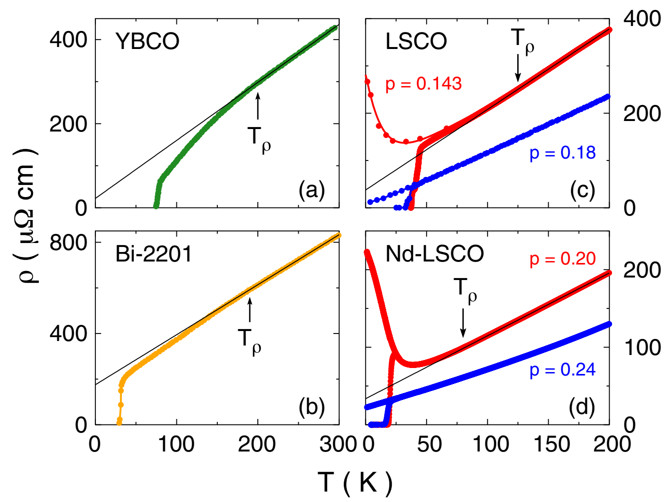

FIG. 5. Resistivity $\rho(T)$ as a function of temperature for four cuprate materials: (a) YBCO at $p = 0.13$ [12]; (b) Bi-2201, underdoped with $T_c = 27$ K [14]; (c) LSCO at $p = 0.143$ (red; [11]); and $p = 0.18$ (blue; [10]) (d) Nd-LSCO at $p = 0.20$ (red) and $p = 0.24$ (blue) [2]. The black line is a linear fit of the high-temperature region and a zoom enables the extraction of T_ρ(arrow), the temperature below which $\rho(T)$ deviates from this linear dependence—a standard criterion for the pseudogap temperature $T^\star$. For LSCO (c) and Nd-LSCO (d), the comparison between two dopings on either side of the pseudogap critical point $p^\star$ reveals the effect on $\rho(T)$ of the drop in carrier density (from $n = 1 + p$ to $n = p$) caused by the pseudogap present at $p < p^\star$ [3,11].

(at $p > p^\star$) to $n = p$ (at $p < p^\star$) [3,6,11]. The consequence is that ρ at $T \to 0$ is larger than it would be without the pseudogap by a factor $\sim(1+p)/p$ [3,11]. This drop in carrier density is what causes the upturn in $\rho(T)$ seen at $T \to 0$ in LSCO [Fig. 5(c)] [9,11], Bi-2201 [38], and Nd-LSCO [Fig. 5(d)] [2,3], when superconductivity is suppressed by a large magnetic field. In Bi-2201, in addition to a pronounced upturn as $T \to 0$ [38], $\rho(T)$ also exhibits a (slight) downturn below $T^\star$ [Fig. 5(b)] [12,14] showing that the two effects of the pseudogap—loss of inelastic scattering and loss of carrier density—do co-exist.

In order to see an upturn in $\rho(T)$ starting right at $T^\star$, the loss of inelastic scattering (causing a downturn) must be a small effect compared to the loss of carriers (causing an upturn). This is the case in sufficiently disordered samples. A nice demonstration of this can be seen in YBCO at $p = 0.18$. In clean samples, $T_\nu = 140 \pm 10$ K from the Nernst coefficient (Fig. 3), but little is seen in $\rho(T)$ across $T^\star$. However, in a disordered sample at the same doping, a clear *upturn* is observed in $\rho(T)$, beginning at $T_\rho = 130 \pm 10$ K (open circle in Fig. 3) [37]. This upturn is definitely due to the pseudogap since no upturn is observed in $\rho(T)$ when $p > p^\star$, even for disorder levels large enough to entirely suppress superconductivity [39]. Calculations without vertex corrections, perhaps appropriate when disorder scattering dominates, do get an upturn in the resistivity [40].

In summary, the Nernst effect is a sensitive probe of the pseudogap phase because a key property of that phase is a loss of carrier density n [6], and $\nu/T \sim 1/n$. Because the pseudogap also causes a drop in inelastic scattering, the two effects reinforce each other in the Nernst signal, since $\nu/T \sim 1/\Gamma$, while they oppose each other in the resistivity, since $\rho \sim \Gamma/n$. The Nernst effect is also an unambiguous probe of $T^\star$ in YBCO, because here the quasiparticle and superconducting contributions to the Nernst signal have opposite sign (Fig. 7). (Note that an early proposal for the negative Nernst signal in YBCO as being due to the CuO chains in that material [41] turns out to be incorrect, as the very same negative signal is observed in the tetragonal material Hg1201 [21], which is free of such chains.)

The resulting phase diagram of YBCO is shown in Fig. 3, where the boundary of the pseudogap phase is clearly delineated (dashed red line). It decreases linearly with doping up to $p \simeq 0.18$ and then drops rapidly to reach its critical point at $p^\star = 0.195$ (red diamond). The aprupt drop of $T^\star$ at $p^\star$ could reflect a first-order transition, as found in some calculations [42]. It is instructive to compare $T_\nu = T_\rho$ in YBCO with the pseudogap temperature $T^\star$ measured by spectroscopic means in Bi-2212. In Fig. 3, we plot as a gray band the value of $T^\star$ vs p measured in Bi-2212 by ARPES, SIS tunneling, STS, and NMR [15]. We see that the $T^\star$ line is essentially the same in YBCO and Bi-2212, two bilayer cuprates with similar T_c domes. The only difference is in the value of $p^\star$ in the normal state, namely $p^\star = 0.195 \pm 0.005$ in YBCO and $p^\star = 0.22 \pm 0.1$ in Bi-2212 [19].

V. LSCO, Nd-LSCO, and Eu-LSCO

We now turn to a different family of cuprates, based on La_2CuO_4. Three materials will be discussed: LSCO, Nd-LSCO, and Eu-LSCO. In all three materials, the quasiparticle Nernst signal in the pseudogap phase at low temperature is positive, therefore of the same sign as the superconducting signal.

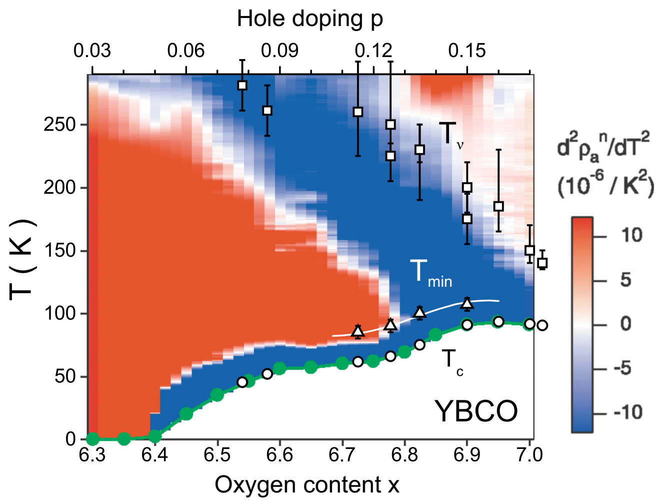

FIG. 6. Resistivity curvature map from Ando *et al.* [12] showing the second temperature derivative of their resistivity data on YBCO, plotted as a function of temperature (vertical axis) and oxygen doping x (bottom horizontal axis). The green dots mark T_c. The top axis shows the approximate hole doping p, estimated from the T_c values [34]. White regions correspond to linear, blue ones to sublinear (downward; $d^2\rho/dT^2 < 0$) and red ones to superlinear (upward; $d^2\rho/dT^2 > 0$) behavior of resistivity with temperature. The boundary of the pseudogap region ($T^\star$) is the lower limit of the white region in the upper right corner. T_ν, T_{min}, and T_c from present work and data of Ref. [20] are added respectively as open squares, triangles, and circles. T_ν points agree reasonably well with the resistivity criterion (as in Fig. 3). The narrow blue region that tracks T_c represents the paraconductivity regime where resistivity drops due to superconducting fluctuations just above T_c. T_{min} (triangles), our criterion for the onset of significant superconducting fluctuations in the Nernst effect, is seen to agree with the onset of paraconductivity, clearly observable at $x < 6.8$ (or $p < 0.13$).

As illustrated in Fig. 7, this makes it more difficult than in YBCO to separate the two contributions, and this difficulty is what led to early misinterpretations of the positive Nernst signal detected in LSCO up to 150 K as being due to vortex-

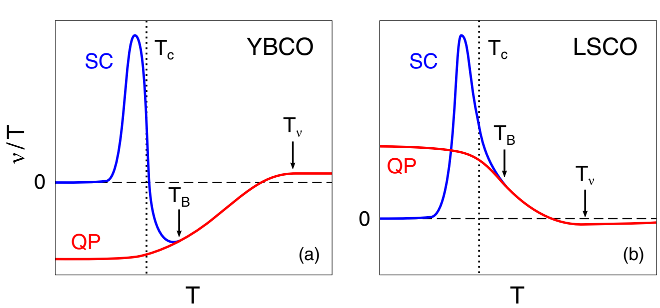

FIG. 7. Cartoon illustrating the behavior of the Nernst coefficient ν in cuprate superconductors, plotted as ν/T vs T. The quasiparticle signal (QP, red) goes from small at high T to large at low T, with a change of sign. It is independent of magnetic field. The change occurs upon entering the pseudogap phase, by crossing below a temperature $T_\nu = T^\star$ (arrow). In YBCO (and Hg-1201), ν is positive at high T (left panel), while in LSCO (and Nd/Eu-LSCO), ν is negative at high T. The superconducting signal (SC, blue) develops below a temperature T_B (arrow) slightly above the zero-field T_c (vertical dotted line). It is always positive and it is suppressed by a magnetic field.

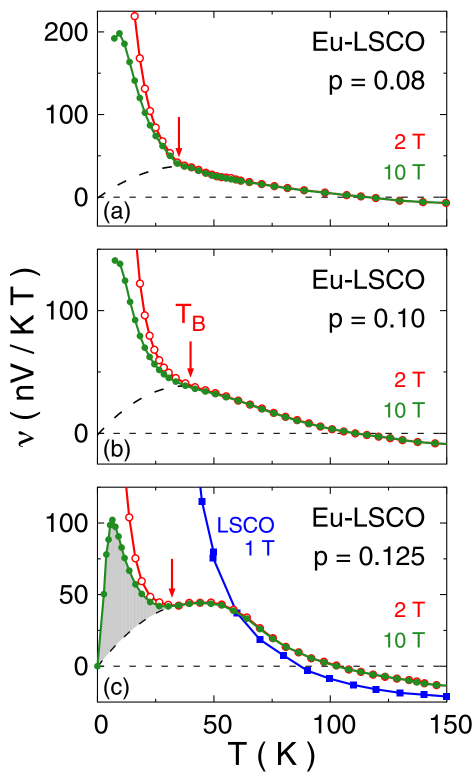

FIG. 8. Nernst coefficient ν of Eu-LSCO at dopings $p = 0.08$ (a), 0.10 (b) and 0.125 (c) versus T, at $H = 2$ T (open red circles) and 10 T (filled green circles). The data at $p = 0.125$ are taken from Ref. [30]. A two-peak structure is seen clearly at $p = 0.125$. At the other two dopings, it shows up as a breaking point in the slope of the data, at $T \simeq 35$ K. This two-peak structure reveals the two distinct contributions to the Nernst effect: one from superconducting fluctuations, seen as a narrow positive peak at low temperature (grey shading in bottom panel), and the other from quasiparticles, seen as a broad positive peak at higher temperature. The dashed line is a guide to the eye for delimiting the quasiparticle peak. In panel (c), we also plot LSCO data at $p = 0.12$ and $H = 1$ T (blue; from Ref. [27]), for comparison. In LSCO, we see that the two separate contributions flow smoothly one into the other. The red arrow marks T_B, the temperature above which the field dependence of ν becomes negligible, the signature of a negligible superconducting signal.

like excitations in underdoped samples with $T_c \simeq 0$ [43]. We discuss this issue in more detail in the Appendix.

Nernst data taken on single crystals have been reported for Nd-LSCO at $p = 0.20$ and 0.24 and for Eu-LSCO at $p = 0.125$ and 0.16 [30]. The new data reported here were taken on Eu-LSCO at $p = 0.08$, 0.10 and 0.21, and on Nd-LSCO at $p = 0.20$ and 0.21. We start by reviewing published data on Eu-LSCO at $p = 0.125$ (from Ref. [30]), displayed in Fig. 8(c), as their double-peak structure reveals most clearly the presence of two separate contributions to the Nernst signal $\nu(T)$: 1) a narrow positive peak at low temperature (shaded in gray), attributed to superconducting fluctuations because of its strong field dependence; 2) a broad positive peak at higher temperature, attributed to quasiparticles because it is independent of field. By applying a magnetic field of 28 T, the superconducting peak is entirely suppressed and only the quasiparticle peak remains (dashed line) [28].

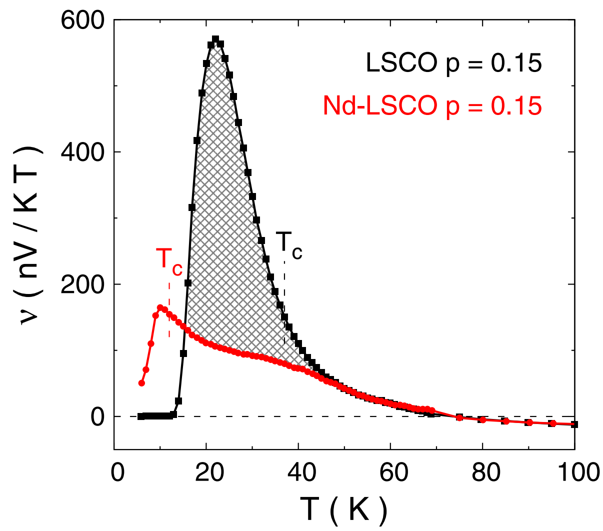

FIG. 9. Nernst coefficient ν of Nd-LSCO (red circles) and LSCO (black squares) at $p = 0.15$, as a function of temperature (data from Ref. [44], at $H = 9$ T). Down to 50 K or so, the two data sets are virtually identical (see also Fig. 13). Note the small anomaly in the Nd-LSCO data at $T \simeq 70$ K, due to the LTT transition, a structural transition not present in LSCO. Below 50 K, the superconducting signal in LSCO starts to deviate upwards. The difference between the two curves (cross-hatched region) is attributable to their different T_c values (37 K and 12 K); it is the superconducting contribution to the Nernst signal in LSCO.

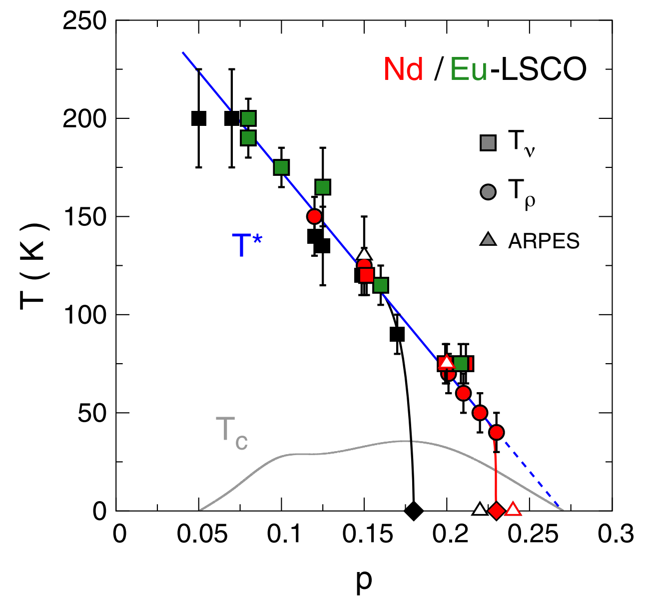

FIG. 10. Temperature-doping phase diagram of LSCO (black), Nd-LSCO (red), and Eu-LSCO (green), showing the pseudogap temperature $T^\star$ (blue line) and the superconducting transition temperature T_c (of LSCO, gray line). T_ν (filled squares, from this work and Refs. [27,30,43–45]) is the temperature below which the quasiparticle Nernst signal starts to increase toward large positive values (Fig. 15). T_ρ (filled circles, from Refs. [2,3,46]) is the temperature below which the resistivity $\rho(T)$ deviates from linearity (Fig. 5). The open triangles show $T^\star$ detected by ARPES as the temperature below which the antinodal pseudogap opens, in LSCO (black) [47] and Nd-LSCO (red) [5]. We see that $T_\nu \simeq T_\rho \simeq T^\star$, within error bars. Note how the pseudogap phase comes abruptly to an end, at a critical doping $p^\star = 0.18 \pm 0.01$ for LSCO (black diamond) [10,11], and at a much higher doping, $p^\star = 0.23 \pm 0.01$, for Nd-LSCO (red diamond) [2,3]. The dashed blue line is a linear extension of the solid blue line.

A double-peak structure is also observed in Nd-LSCO at $p = 0.15$ [44] (see Fig. 9) and in the electron-doped cuprate PCCO at $x = 0.13$ [29]. In all cases, the two peaks in $\nu(T)$ can be resolved because T_c is sufficiently low, roughly 10 K. By contrast, in LSCO at $p = 0.12$ ($p = 0.15$), where $T_c \simeq$ 30 K (37 K), the superconducting peak in ν is moved up in temperature so that it lies on top of the quasiparticle peak [Figs. 8(c) and 9]. This unfortunate overlap is what led to the initial misinterpretation of the LSCO data by the Princeton group [43,45].

Even when two peaks cannot be resolved, one can still identify a temperature T_B above which the Nernst coefficient is independent of magnetic field, a good indication that the superconducting Nernst signal is negligible. In Fig. 8, we see that the Nernst signal at 2 T splits off from the 10 T data below $T_B \simeq 30$–40 K, for all three dopings. Above T_B, the Nernst signal is therefore all due to quasiparticles, to a good approximation, and this is the signal we will use to pin down the onset temperature $T^\star$ of the pseudogap phase in the three LSCO-based cuprates.

It is convenient to begin with Nd-LSCO, whose temperature-doping phase diagram is shown in Fig. 10 (red symbols), because its properties in the vicinity of the critical doping $p^\star$ below which the pseudogap phase appears at $T = 0$ (red diamond) have been thoroughly characterized. In particular, ARPES measurements establish that the antinodal pseudogap in Nd-LSCO opens below a temperature $T^\star = 75 \pm 5$ K at $p = 0.20$ (white triangle, Fig. 10), and that there is no pseudogap at $p = 0.24$ [5].

The onset of the pseudogap phase has a dramatic impact on the electrical resistivity of Nd-LSCO [2], as seen in Fig. 5(d). At $p = 0.24$, where there is no pseudogap, the normal-state $\rho(T)$ (measured in high fields) is linear from $T \simeq 80$ K down to $T \simeq 0$ [2,3]. At $p = 0.20$, $\rho(T)$ undergoes a huge upturn as $T \to 0$, increasing its value by a factor ~6 relative to the value ρ_0 it would have in the absence of a pseudogap [2,3]. We define T_ρ as the temperature where the upturn starts, relative to the linear-T dependence observed at higher temperature [2,3]. Using this definition, resistivity data yield the six red circles in Fig. 10 [2,3]. At $p = 0.20$, $T_\rho = 70 \pm 10$ K, so that $T_\rho = T^\star$, within error bars, thereby confirming the interpretation of the low-T upturn in $\rho(T)$ as being due to the pseudogap.

Using measurements of both the in-plane and out-of-plane (c-axis) resistivities, the upturn in $\rho(T)$ was tracked vs doping to pinpoint the precise location of the critical point [3,4] at $p^\star \simeq 0.23 \pm 0.01$ (red diamond in Fig. 10). This type of upturn was first detected in LSCO twenty years ago, as illustrated in Fig. 5(c) [9]. Its origin was only recently shown to be a drop in the carrier density from $n = 1 + p$ above $T^\star$ to $n = p$ at $T = 0$, combined with a negligible change in carrier mobility μ [11]. In Nd-LSCO, this interpretation is confirmed by Hall effect measurements that indeed find a drop in the $T = 0$ Hall number from $n_H \simeq 1 + p$ above $p^\star$ to $n_H \simeq p$ below $p^\star$ [2,3], as observed in YBCO [6].

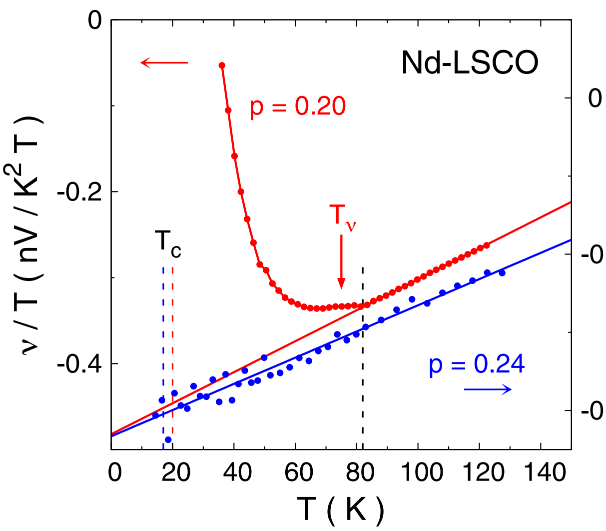

FIG. 11. Nernst coefficient ν of Nd-LSCO at $p = 0.20$ (left axis, red dots, $H = 16$ T; this work) and $p = 0.24$ (right axis, blue dots, $H = 10$ T [30]), plotted as ν/T vs T. The red and blue vertical dashed lines mark T_c ($H = 0$ T) at $p = 0.20$ (20 K) and 0.24 (17 K), respectively. The black vertical dashed line marks the transition to the low-temperature tetragonal (LTT) structure, at $T_{LTT} = 82$ K for $p = 0.20$; the transition only causes a small kink in the (red) data (see also Fig. 9). The solid color-coded lines are linear fits to the data above 82 K, extended down to $T = 0$. This comparison shows the effect of the pseudogap on the Nernst coefficient: a large upturn below $T_\nu = T^\star$ (red arrow) at $p = 0.20 < p^\star$, in contrast with the continuous linear decrease at $p = 0.24 > p^\star$.

The large and abrupt drop in n below $p^\star$ should cause ν/T to increase, just as ρ and R_H do, since all three quantities go as $1/n$ (at $T = 0$). This is indeed the case. (A large enhancement of ν, from small and negative to large and positive, is also found in calculations of Fermi-surface reconstruction by commensurate [48] and incommensurate [49] antiferromagnetic order.) In Fig. 11, we show Nernst data for Nd-LSCO at $p = 0.20$ and $p = 0.24$, plotted as ν/T vs T. The data in this figure are limited to those temperatures where no field dependence is detected and are therefore purely a quasiparticle signal. The difference in behavior is striking. At $p = 0.24$, ν/T decreases linearly as $T \to 0$, down to at least 15 K, remaining negative all the way. This is analogous to the linear-T decrease in $\rho(T)$ at that doping [Fig. 5(d)]. The value ν/T extrapolates to at $T = 0$, -0.42 nV/K^2 T, is in reasonable agreement with expectation. Indeed, using the second term in Eq. (1), we estimate $\nu/T = -\mu S/T$ at $T \to 0$, with the mobility $\mu = (\rho_{xy}/H)/\rho_{xx}$, to yield $\nu/T = -0.6$ nV/K^2 T, given that $S/T = +0.3$ μV/K^2 [50] and $\mu = +0.002$ T^{-1} [3] in Nd-LSCO at $p = 0.24$. The fact that the measured ν/T is slightly less negative than the calculated one means that the first (positive) term in Eq. (1) acts to partially reduce its magnitude. In the end, $\nu/T \simeq -(\frac{2}{3})\mu S/T$, the value given by the simple formula in Eq. (2), since $S/T \approx (\pi^2/2)(k_B^2/e)(1/\epsilon_F)$. All this means that in Nd-LSCO at $p = 0.24$, just as the small (positive) Hall coefficient reflects the large holelike Fermi surface, with a Hall number equal to the carrier density ($n_H = 1 + p$) [2], so do the small Seebeck and Nernst coefficients.

At $p = 0.20 < p^\star$, ν/T also decreases linearly down to 80 K, with a similar slope, but below 80 K, it undergoes a dramatic rise to positive values (Fig. 11). This upturn in ν/T is analogous to the upturn in $\rho(T)$ at that doping [Fig. 5(d)]. It is a second signature of the pseudogap phase. In other words, just as the parallel drops in $\rho(T)$ and ν/T observed in YBCO are two signatures of $T^\star$, so the parallel rises in $\rho(T)$ and ν/T observed in Nd-LSCO are the signature of $T^\star$ in that material—confirmed in this case by a direct spectroscopic measurement [5]. Note that in our previous work on the Nernst effect in Nd-LSCO [30] we attributed the rise in the Nernst coefficient at $p = 0.20$ to the onset of stripe order (combined charge-density and spin-density waves) at low temperature. (Note that no charge order has been detected at $p = 0.20$, but spin order is seen by neutron diffraction below 20 K [51], with a slowing down of spin fluctuations detected by NQR below 40 K [52].) The recent ARPES study showing a pseudogap opening at 75 K [5], precisely where the upturn in $\rho(T)$ [3] and in ν/T (Fig. 11) begins, has clarified the cause of the upturns.

Upon close inspection of the Nernst data on Nd-LSCO $p = 0.20$ (Fig. 11), we see a small kink at $T = 82$ K, due to the structural transition into the low-temperature tetragonal (LTT) phase. To ascertain that this transition has only a small effect on the large upturn in ν/T, we compare Nernst data in the three LSCO-based cuprates, at three different dopings. In Fig. 12, we compare our own data at $p = 0.21$ on Nd-LSCO and Eu-LSCO. In our Nd-LSCO sample, there is a clear kink in $\rho(T)$ at $T_{LTT} = 84$ K (red dotted line). In Eu-LSCO, the LTT transition

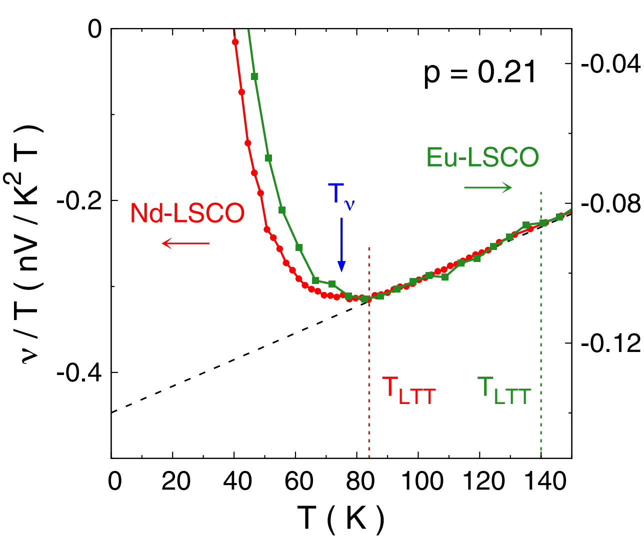

FIG. 12. Nernst coefficient ν of Nd-LSCO (red circles; left axis; $H = 16$ T) and Eu-LSCO (green squares; right axis; $H = 10$ T), both at $p = 0.21$, plotted as ν/T versus T. Above 40 K, ν is independent of magnetic field. Vertical dotted lines mark the structural transitions to the LTT structure at low T. The black dashed line is a linear fit to the Nd-LSCO data above 85 K, extended down to $T = 0$. Eu-LSCO data also show linearity in the same temperature range. Data deviate upwards from the linear fit below a temperature $T_\nu = 75 \pm 10$ K for Nd-LSCO (blue arrow) and $T_\nu = 75 \pm 10$ K for Eu-LSCO. The very different LTT temperatures of the two materials implies that the upturn in ν/T observed at roughly the same temperature in both is not caused by this structural transition, but instead by the pseudogap opening.

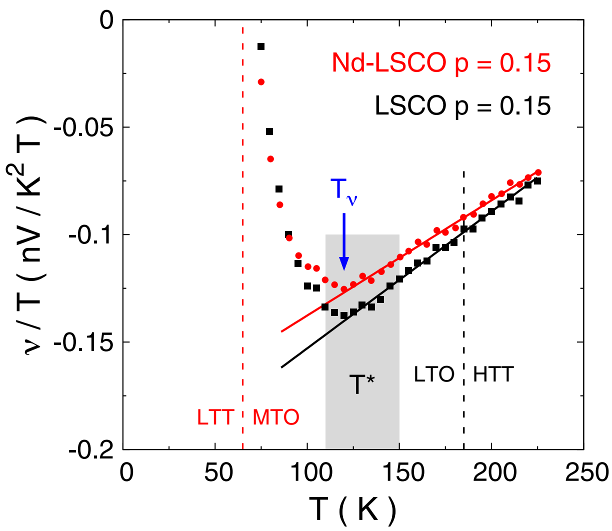

FIG. 13. Nernst coefficient ν of Nd-LSCO (red circles) and LSCO (black squares) at $p = 0.15$, plotted as ν/T versus T (data from Ref. [44]). Vertical dashed lines indicate structural transition temperatures: from middle-temperature orthorhombic (MTO) to low-temperature tetragonal (LTT) in Nd-LSCO (70 K [53], Fig. 9), and from high-temperature tetragonal (HTT) to low-temperature orthorhombic (LTO) in LSCO (185 K [54]). One can see that the simultaneous rise in ν/T below $T_\nu = 120 \pm 10$ K (blue arrow) in the two materials cannot be caused by their structural transitions, which take place well below and above, respectively. The gray band marks the location of the pseudogap temperature measured by ARPES in LSCO at $p = 0.15$ [47], at $T^\star = 130 \pm 20$ K.

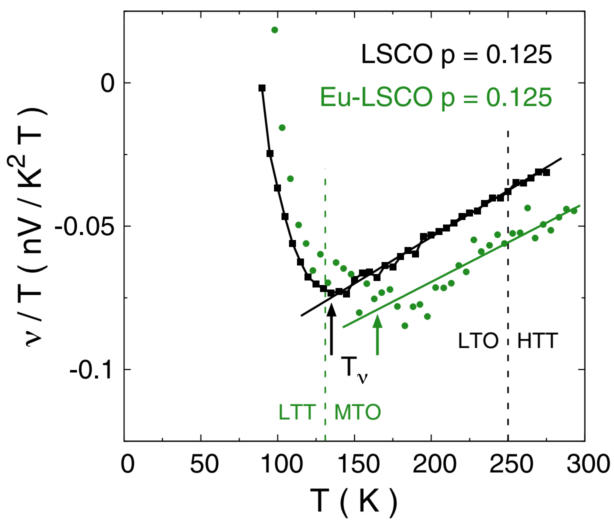

FIG. 14. Nernst coefficient ν of Eu-LSCO (green circles; from Ref. [55]) and LSCO (black squares; from Ref. [44]) at $p = 0.125$, plotted as ν/T versus T. Vertical dashed lines indicate structural transition temperatures: from middle-temperature orthorhombic (MTO) to low-temperature tetragonal (LTT) in Eu-LSCO (131 K [56]), and from high-temperature tetragonal (HTT) to low-temperature orthorhombic (LTO) in LSCO (250 K [54]). As in Figs. 12 and 13, the rise in ν/T below $T_\nu = 165 \pm 20$ K for Eu-LSCO and $T_\nu = 135 \pm 20$ K for LSCO is unrelated to their structural transitions.

at $p = 0.21$ is expected at $T_{\mathrm{LTT}} \simeq 140$ K [56] (green dotted line). However, it has no detectable signature in our sample; even the c-axis resistivity shows no feature whatsoever. Be that as it may, any structural transition in Eu-LSCO at $p = 0.21$ occurs well above 80 K. Yet, in both samples the Nernst data show very similar upturns. We define T_ν as the temperature where the upturn in ν/T vs T begins. At $p = 0.21$, we find $T_\nu = 75 \pm 10$ K in Nd-LSCO and $T_\nu = 75 \pm 10$ K in Eu-LSCO; those values are added to the phase diagram (squares; Fig. 10).

In Fig. 13, we compare data at $p = 0.15$ on Nd-LSCO and LSCO (from Ref. [44]). We see that the upturn in ν/T starts at a higher temperature than it did at $p = 0.21$, with $T_\nu = 120 \pm 10$ K not only in Nd-LSCO but also in LSCO. The two samples exhibit essentially identical behavior, even though their respective crystal structures and structural transitions are quite different: The LTT transition in Nd-LSCO is at $T_{\mathrm{LTT}} = 70$ K [53] (red dashed line), 50 K below T_ν, while the LTO transition in LSCO is at $T_{\mathrm{LTO}} \simeq 185$ K [54] (black dashed line), 65 K above T_ν. This shows that the large upturns in ν/T are not caused by structural transitions. Instead, they are caused by the opening of the pseudogap, as confirmed also in LSCO by ARPES measurements at $p = 0.15$, which yield $T^\star = 130 \pm 20$ K (gray band in Fig. 13) [47]. As we did at $p = 0.20$, we again find that $T_\nu = T_\rho = T^\star$ at $p = 0.15$, within error bars (Fig. 10).

This conclusion is reinforced by yet another comparison, at $p = 0.125$, between Eu-LSCO (from Ref. [55]) and LSCO (from Ref. [44]), as displayed in Fig. 14. We see that in Eu-LSCO the upturn in ν/T now starts above the LTT transition at $T_{\mathrm{LTT}} = 131$ K (green dotted line), whereas it started well below it at $p = 0.21$ (Fig. 12). In other words, the $T^\star$line in Eu-LSCO goes through the LTT transition unperturbed, as in Nd-LSCO (Fig. 10). Similarly, the structural transition in LSCO has no effect on $\nu(T)$ and $T^\star$ is well below.

In Fig. 15, we collect data at several dopings for all three materials. We see that the behavior is similar in all three: the upturn at low T in ν/T onsets at a temperature T_ν (arrows) that increases monotonically with decreasing p. In Fig. 10, all values of T_ν are plotted on a common phase diagram. The first thing to note is that $T_\nu(p)$ is the same in all three materials, within error bars, across the whole phase diagram.

In Fig. 10, we also plot T_ρ in Nd-LSCO [2,46] (red circles), the temperature below which $\rho(T)$ deviates from its linear dependence at high temperature, as illustrated in Fig. 5(d). (This is the same definition used for YBCO, except that here the deviation is upward instead of downward.) We see that $T_\nu = T_\rho$, within error bars, as also found in YBCO (Fig. 3).

In Fig. 16, the T_ν values for LSCO, Nd-LSCO, and Eu-LSCO are plotted on the curvature map of Ando and coworkers for LSCO [12]. They are seen to coincide reasonably well with the upper boundary of the red region, where the upward deviation in $\rho(T)$ begins. Note that in LSCO the (white) region of linear-T behavior is contaminated near its lower bound by the structural transition, seen clearly as the red ridge inside the white region. This anomaly in $\rho(T)$ can be mistaken for the pseudogap phase boundary in a resistive determination of $T^\star$. By contrast, a determination based on the Nernst coefficient is clear (Fig. 13), and it shows that the $T^\star(p)$ line in LSCO lies well below its structural transition (Fig. 16).

In Fig. 16, the region of paraconductivity, in which superconducting fluctuations cause a decrease in $\rho(T)$ above T_c,

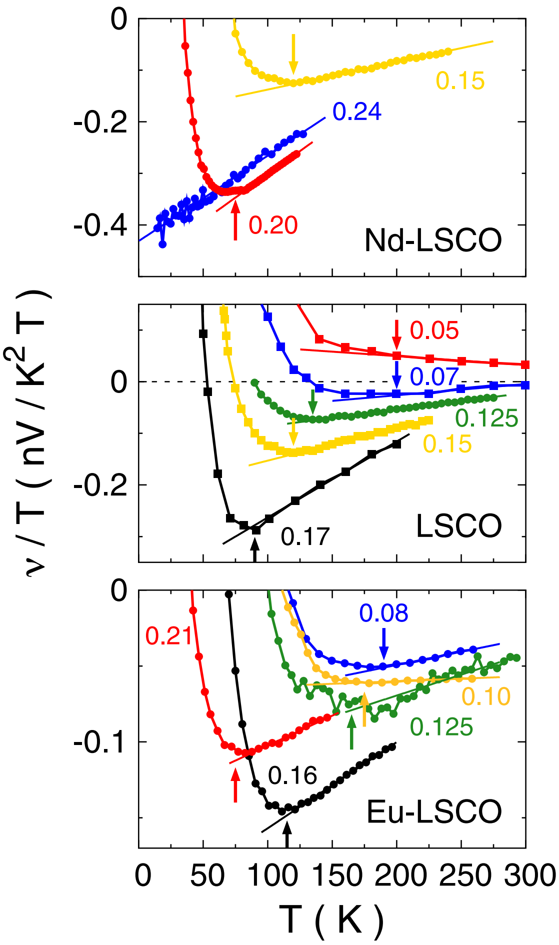

FIG. 15. Nernst coefficient ν of Nd-LSCO (top), LSCO (middle), and Eu-LSCO (bottom), at various dopings as indicated, plotted as ν/T versus temperature. Lines are linear fits of the data at high temperature. Arrows mark the temperature T_ν below which the data start to deviate upward from linearity (see Figs. 11–14 for a zoomed view of the data from which we can more easily identify T_ν). The values of T_ν are (from low to high p): $T_\nu = 120 \pm 10$, 75 ± 10, and 0 K in Nd-LSCO, $T_\nu = 200 \pm 25$, 200 ± 25, 135 ± 10, 120 ± 10, and 90 ± 10 K in LSCO, and $T_\nu = 190 \pm 10$, 175 ± 10, 165 ± 20, 115 ± 10, and 75 ± 10 K in Eu-LSCO. All values of T_ν are plotted on the phase diagram of Fig. 10. Nd-LSCO with $p = 0.15$, LSCO with $p = 0.15$, and $p = 0.125$ were measured at 9 T (from Ref. [44]); Nd-LSCO with $p = 0.20$ and Eu-LSCO with $p = 0.21$ at 16 T (present work); Nd-LSCO with $p = 0.24$, Eu-LSCO with $p = 0.16$ (from Ref. [30]), Eu-LSCO with $p = 0.08$ and 0.10 (present work), and Eu-LSCO with $p = 0.125$ (from Ref. [55]) at 10 T; LSCO with $p = 0.17$ at 8 T (from Ref. [43]) and LSCO with $p = 0.05, 0.07$ (from Ref. [45]) at $H \to 0$.

shows up very clearly as a blue band tracking the T_c dome, of width 30 K or so. We also plot T_B in LSCO (white diamonds), the temperature above which ν is independent of field (see Fig. 22). It agrees well with the upper limit of paraconductivity, both saying that superconducting fluctuations have a negligible impact on either resistivity or Nernst above $\sim T_c + 30$ K or so. The long-held notion that superconducting fluctuations are detected in LSCO up to $\sim T_c + 100$ K is incorrect (see the Appendix for further discussion).

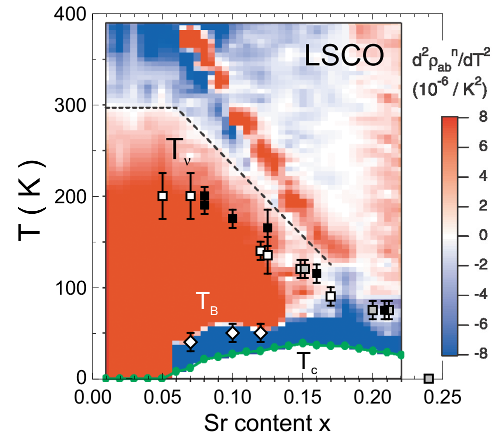

FIG. 16. Resistivity curvature map from Ando *et al.* [12] showing the second temperature derivative of their resistivity data on LSCO, with T_c as solid green circles. As in Fig. 6, regions in white correspond to linear, in blue to sublinear (downward; $d^2\rho/dT^2 < 0$) and in red to superlinear (upward; $d^2\rho/dT^2 > 0$) behavior of resistivity with temperature. The red ridge inside the white region is due to the HTT-LTO structural transition in LSCO. The boundary of the pseudogap phase ($T^\star$) is the lower border of the white region (the dashed line is a guide to the eye). Our data points for T_ν from Fig. 10 are added, for Nd-LSCO (gray squares), Eu-LSCO (black squares), and LSCO (open squares). The T_ν data points agree reasonably well with the start of the upturn in the resistivity (as in Fig. 10). The narrow blue region that tracks T_c is due to paraconductivity. The values of T_B for LSCO are added as open diamonds (from Fig. 22). They agree well with the onset of paraconductivity. Together they delineate the regime of significant superconducting fluctuations in LSCO, limited to 30 K above T_c.

In order to complete our determination of the pseudogap phase boundary in LSCO, we need to know the location of $p^\star$, its end point at $T = 0$. High-field measurements of the resistivity of LSCO reveal that $\rho(T)$ is perfectly linear below 70 K or so, down to the lowest T, at $p = 0.23$, $p = 0.21$, and even $p = 0.18$ [10]. At $p = 0.17$ and lower dopings, however, an upward deviation from linearity is observed at low T [9]. Just as the appearance of an upturn was used to locate $p^\star = 0.23 \pm 0.01$ in Nd-LSCO, we find that $p^\star = 0.18 \pm 0.01$ in LSCO (black diamond, Fig. 10).

In summary, the onset of the pseudogap phase at $T^\star(p)$ causes an upturn in ν/T in the three La_2CuO_4-based cuprates, which coincides with the upturn in $\rho(T)$, it has nothing to do with structural transitions, and it is distinct from the upturn due to superconducting fluctuations close to T_c. In the $T - p$ phase diagram (Fig. 10), the three materials are found to have the same $T^\star(p)$ line, decreasing monotonically with p. However, the pseudogap phase ends sooner in LSCO, at $p^\star = 0.18$, than in Nd-LSCO (or Eu-LSCO), where it extends up to $p^\star = 0.23$.

VI. DISCUSSION

We have shown that it is possible to disentangle the superconducting and quasiparticle contributions to the Nernst coefficient $\nu(T)$ in cuprates. The key difference is that the former depends strongly on magnetic field and not the latter. In YBCO, they are also of opposite sign. We then showed that the

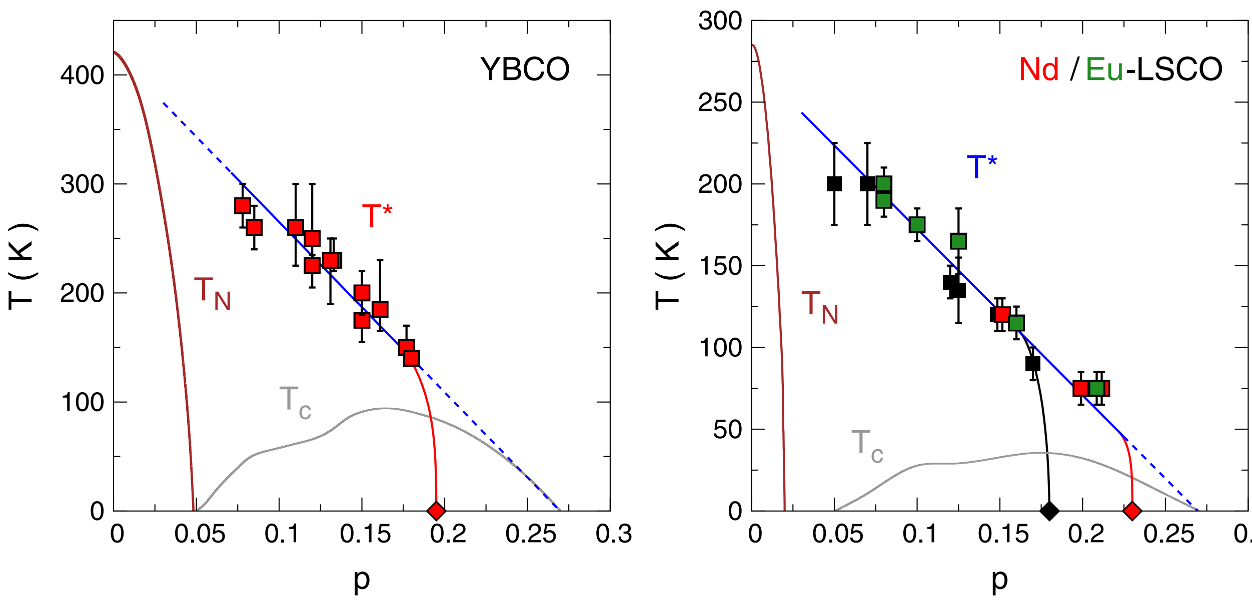

FIG. 17. Temperature-doping phase diagrams of YBCO (a) and Nd/Eu-LSCO (b) showing the pseudogap temperature $T^\star$ (T_ν, squares), the Néel temperature T_N (brown line), and the superconducting transition temperature T_c (gray line). The blue line is a linear guide to the eye showing that $T^\star$ extrapolates to T_N at half filling on the underdoped side ($p = 0$) while it merges with T_c on the overdoped side where superconductivity disappears. Note that the $T^\star$ line of YBCO is proportional to but higher than that of LSCO: $T^\star_{\rm YBCO} \simeq 1.5 T^\star_{\rm LSCO}$. Roughly the same scaling applies to T_N at $p = 0$: $T_N^{\rm YBCO}(0) \simeq 450$ K [57] and $T_N^{\rm LSCO}(0) \simeq 280$ K [54]. Diamonds mark the pseudogap critical points for YBCO (red) at $p^\star = 0.195 \pm 0.005$ [6], LSCO (black) at $p^\star = 0.18 \pm 0.01$ [10,11], and Nd-LSCO (red) at $p^\star = 0.23 \pm 0.01$ [3]. T_ν are taken from Fig. 3 for YBCO and from Fig. 10 for LSCO; T_N is taken from Ref. [57] for YBCO and from Ref. [58] for LSCO.

quasiparticle Nernst signal in Nd-LSCO and LSCO undergoes a pronounced change when temperature is reduced below $T^\star$, the onset temperature of the pseudogap phase established by ARPES measurements. A similar, albeit smaller, change in the resistivity $\rho(T)$ occurs simultaneously. The onset of these changes, at T_ν and T_ρ respectively, can therefore be used to define $T^\star$. Using new and published Nernst data in four cuprates—YBCO, LSCO, Nd-LSCO, and Eu-LSCO—we identify T_ν at various dopings and then map $T^\star$ across the temperature-doping phase diagram, in Fig. 3 for YBCO and in Fig. 10 for the other three. We find that the latter three materials all have the same $T^\star(p)$ line (up to $p \simeq 0.17$), irrespective of their different structural transitions.

A. Boundary of the pseudogap phase

Having delineated the boundary $T^\star(p)$ of the pseudogap phase, the question arises: Is it a transition or a crossover? Detailed studies of the pseudogap opening via ARPES show a rather sharp onset with decreasing temperature, as in optimally-doped Bi-2201 [14] and Nd-LSCO at $p = 0.20$ [5], pointing to a transition. By contrast, the change in $\rho(T)$ across $T^\star$ is always very gradual (Fig. 5), suggestive of a crossover. The change in $\nu(T)$ is also rather gradual when $T^\star$ is high, but it does get sharper when $T^\star$ is lower (Fig. 15). In the normal state at $T \to 0$, the drop in Hall number n_H across $p^\star$ (in either YBCO or Nd-LSCO) is as sharp as expected theoretically for a quantum phase transition into a phase of long-range antiferromagnetic order [3]. In Nd-LSCO, the upturn in $\rho(T)$ appears very rapidly upon crossing below $p^\star$, going from no upturn to full upturn over a doping interval of relative width $\delta p / p^\star \simeq 0.06$ [3].

To better compare the phase diagrams of YBCO and LSCO, we display them side by side in Fig. 17. Some general features are immediately apparent.

1. Pseudogap temperature $T^\star$

$T^\star$ decreases monotonically with p, in both cases. We see that the pseudogap temperature is 1.5 times larger in YBCO (and Bi-2212) than in LSCO (and Nd-LSCO and Eu-LSCO): $T^\star_{\rm YBCO} \simeq 1.5 T^\star_{\rm LSCO}$ (up to $p \simeq 0.17$). This is an important quantitative fact, which may reflect the strength of interactions and possibly the pairing strength. The weaker maximal T_c of LSCO (40 K) compared to YBCO (93 K) may be related to its smaller $T^\star$.

A linear fit to $T^\star$ vs p gives a line that connects $T_N(0)$, the Néel temperature for the onset of commensurate antiferromagnetic order at $p = 0$, to p_{c2}, the upper end of the superconducting dome at $T = 0$ (straight dashed lines in Fig. 17). The slope of that line is 1.5 times larger in YBCO and so is $T_N(0)$: $T_N^{\rm YBCO} \simeq 450$ K [57] and $T_N^{\rm LSCO} \simeq 280$ K [54], at $p = 0$.

These connections suggest a link between the pseudogap phase and the antiferromagnetism of the undoped Mott insulator. They also suggest that the same interactions favor pseudogap formation and pairing.

2. Pseudogap critical doping $p^\star$

If the linear decrease of $T^\star(p)$ with doping continued all the way, $T^\star(p)$ would go to zero at $p \simeq p_{c2}$, the critical doping where T_c goes to zero at high doping. In Fig. 17, we see that this is not the case, and the pseudogap phase instead comes to a rather abrupt end, with $T^\star(p)$ dropping precipitously to

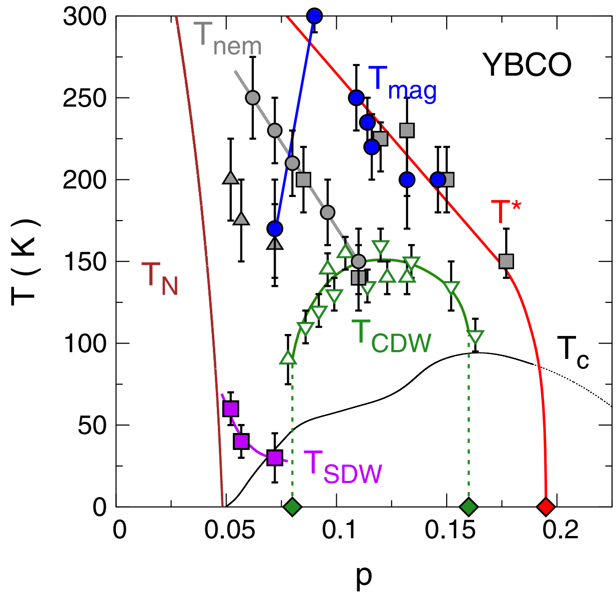

FIG. 18. Temperature-doping phase diagram of YBCO showing the Néel temperature T_N (brown line), the superconducting transition temperature T_c (black line), and the pseudogap temperature $T^\star$ (red line) and critical point $p^\star$ (red diamond), all from Figs. 3 and 17. In addition, we show the charge-density-wave phase (CDW; green), delineated by the temperature T_{CDW} below which short-range CDW correlations are detected by x-ray diffraction (up triangles [69]; down triangles [70]). The two green diamonds mark the critical dopings at which the CDW phase begins ($p_1^{CDW} = 0.08$ [71]) and ends ($p_2^{CDW} = 0.16$ [6]) at $T = 0$ in the absence of superconductivity, as detected by high-field Hall effect measurements. T_{SDW} (purple squares) marks the temperature below which incommensurate short-range spin-density-wave (SDW) correlations are detected by neutron diffraction (in zero field) [72]. Gray symbols mark T_{nem}, the onset temperature of nematicity, an electronic in-plane anisotropy detected in the resistivity (circles [73,74]), the Nernst coefficient (squares [20,74]), and the spin fluctuation spectrum measured by inelastic neutron scattering (triangles [72]). T_{mag} (blue circles) is the onset temperature of intra-unit-cell magnetic order detected by polarized neutron diffraction [75–77]. The blue line highlights the drop in T_{mag} below $p = 0.09$.

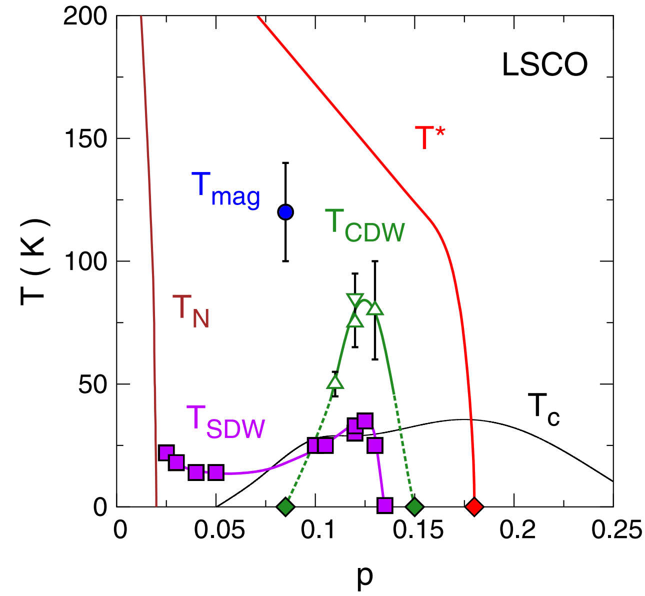

FIG. 19. Temperature-doping phase diagram of LSCO showing the Néel temperature T_N (brown line), the superconducting transition temperature T_c (black line), and the pseudogap temperature $T^\star$ (red line) and critical point $p^\star$ (red diamond), all from Figs. 10 and 17. In addition, we show the charge-density-wave phase (CDW; green), delineated by the temperature T_{CDW} below which short-range CDW correlations are detected by x-ray diffraction (up triangles [78]; down triangles [79]). The two green diamonds mark the critical dopings at which the CDW phase begins ($p_1^{CDW} = 0.085$) and ends ($p_2^{CDW} = 0.15$) at $T = 0$ in the absence of superconductivity, as detected by high-field thermopower measurements [80]. T_{SDW} (purple squares) marks the temperature below which incommensurate short-range SDW order is detected by neutron diffraction [65,81–84]. The blue circle at $p = 0.085$ marks T_{mag}, the onset temperature of intra-unit-cell magnetic order, detected by polarized neutron diffraction [85].

zero at $p^\star$, well below p_{c2}. In Nd-LSCO, $T^\star(p)$ extends up to $p \simeq 0.23$ (Fig. 10), and only then does it drop suddenly to zero at $p^\star = 0.23$ [3,4], slightly (but distinctly) below $p_{c2} \simeq 0.27$. In LSCO, $T^\star(p)$ follows the very same line as in Nd-LSCO, up to $p \simeq 0.16$, but then, in striking contrast, it starts to drop at $p = 0.17$ and goes to zero at $p^\star \simeq 0.18$ (Fig. 17). The difference between those two materials is seen most clearly in their normal-state resistivity (measured to low T in high fields): In Nd-LSCO, $\rho(T)$ shows a huge upturn at $p = 0.20$ and 0.22, for example [3], while in LSCO $\rho(T)$ remains linear down to $T \to 0$ at $p = 0.18$ and 0.21 [10] (see Fig. 5).

This raises a crucial, and largely unexplored question: What controls the location of $p^\star$? Specifically: Why is $p^\star$ so much higher in Nd-LSCO than in LSCO, when $T^\star(p)$ is otherwise the same (below $p \simeq 0.17$)? An answer to these questions could elucidate the fundamental nature of the pseudogap phase. A potential ingredient in the answer is the interesting observation [19] made in Bi-2212 that the end of the pseudogap phase in the normal state (above T_c) coincides with the (Lifshitz) transition that changes the topology of the Fermi surface (in one of the two CuO_2 planes of the bilayer [59]), from holelike below to electronlike above the critical doping $p_{FS} = 0.225$ at which the van Hove singularity crosses the Fermi level [59]. The idea would be that the pseudogap cannot form on an electronlike Fermi surface, i.e., $p^\star \leqslant p_{FS}$. This is consistent with data on LSCO [60] and Nd-LSCO [5] and, to our knowledge, no data on any cuprate contradicts this idea. A recent study of Nd-LSCO shows that the application of hydrostatic pressure reduces $p^\star$ and p_{FS} by the same amount, confirming that the inequality $p^\star \leqslant p_{FS}$ holds [22]. Numerical solutions of the Hubbard model also obtain the inequality $p^\star \leqslant p_{FS}$ [61,62]. This nontrivial agreement between theory and experiment suggests that the pseudogap is due to short-range antiferromagnetic correlations.

B. Orders inside the pseudogap phase

In hole-doped cuprates, a number of phases, sometimes with only short-range order, exist in the underdoped region of the phase diagram. Here we discuss four of the main phases that have been detected experimentally.

1. Spin density wave

Long-range commensurate antiferromagnetic (AF) order dies out quickly with increasing p: T_N goes to zero at the critical doping $p_N = 0.05$ in YBCO and $p_N \simeq 0.02$ in LSCO (Fig. 17). Beyond p_N, incommensurate spin-density-wave (SDW) order is observed at low T, with correlation lengths that vary from rather short to fairly long amongst the various cuprates. In YBCO, short-range SDW order is observed up to $p_{SDW} \simeq 0.07$ in zero field (purple squares, Fig. 18). It stops when charge-density-wave (CDW) order starts, at $p_1^{CDW} \simeq 0.08$, evidence that the two orders compete (arguably because their periods do not match [63]).

In LSCO, SDW order extends up to $p_{SDW} \simeq 0.13$ in zero field (purple squares, Fig. 19), and it coexists with CDW order, evidence that the two orders do not compete (arguably because their periods match [63]). A magnetic field which suppresses superconductivity enhances SDW order in both YBCO and LSCO [64]. In LSCO, a field of 15 T pushes the SDW critical point up to $p_{SDW} \simeq 0.15$ [65]. Extrapolating to higher fields, it is conceivable that $p_{SDW} = p^\star \simeq 0.18$ at $H = H_{c2} \simeq 60$ T.

In other words, when the competing superconductivity is fully suppressed by a field, SDW order in LSCO could extend up to $p^\star$, i.e., the nonsuperconducting ground state of the pseudogap phase could host SDW order. This is supported by μSR studies on LSCO with Zn impurities used to suppress superconductivity, where magnetism is detected up to $p = 0.19 \pm 0.01$ [66–68].

This is also established in the case of Nd-LSCO, where magnetic Bragg peaks are detected by neutron diffraction [51] up to $p = 0.20$ and their onset temperature T_{SDW} and intensity both go to zero at $p \to p^\star = 0.23 \pm 0.01$. In Nd-LSCO, superconductivity is much weaker than in LSCO and a magnetic field is not needed to help SDW order win the competition. Hence the magnetic Bragg peaks do not depend on field [65]. Note, however, that the magnetism in Nd-LSCO at $p = 0.20$ may not be fully static, as it is not detected by μSR [86].

In YBCO, suppressing superconductivity with a large field does not induce SDW order in the range where there is CDW order, i.e., between $p_1^{CDW} = 0.08$ and $p_2^{CDW} = 0.16$ [87]. However, adding Zn impurities to suppress superconductivity, e.g., at $p \simeq 0.12$, also suppresses CDW order, and this nucleates SDW order [88]. In other words, there is a three-way phase competition. It is then conceivable that between p_2^{CDW} and $p^\star$, SDW order could emerge if superconductivity is fully suppressed, as we have discussed above for LSCO. In YBCO, this would require fields of order 150 T, the maximal value of H_{c2} [89].

In summary, magnetic order (AF or SDW) at low T is ubiquitous in hole-doped cuprates and it may well exist at all dopings from $p = 0$ up to $p^\star$ when it is not suppressed by competition from superconductivity or CDW order. It is therefore an important property of the pseudogap phase at $T \to 0$—a second link between pseudogap and antiferromagnetism (the first being $T^\star \simeq T_N$ at $p \to 0$). Having said this, the pseudogap phase is not simply a phase of SDW order, since $T_{SDW} \ll T^\star$ (Figs. 18 and 19).

2. Charge density wave

Twenty years ago, CDW order was first detected in cuprates by neutron diffraction, in Nd-LSCO and LBCO at $p \simeq 0.12$ [92]. Five years later, it was seen via STM in Bi-2212 [93,94]. Another five years later, CDW order was first sighted in YBCO via its effect on the Fermi surface, reconstructed into small electron pockets [71,91,95–98], and then observed directly via NMR [87,99] and x-ray diffraction (XRD) [100,101]. In addition to YBCO, CDW order has been observed by XRD in Nd-LSCO [102,103], Eu-LSCO [56,104], LSCO [78,79], Hg-1201 [105], Bi-2212 [106], and Bi-2201 [107]. It is typically strongest at $p \simeq 0.12$ and confined to a region entirely inside the pseudogap phase, between two critical dopings: p_1^{CDW} at low doping and p_2^{CDW} at high doping. For the four materials of particular focus here, all evidence to date indicates that p_2^{CDW} is well below $p^\star$, (see Table I and Figs. 18 and 19). This immediately implies that the pseudogap phase is not a phase of CDW order, nor is it a high-temperature precursor of that order. This is confirmed by the fact that the onset temperature of CDW order in these same materials is a dome peaked at $p \simeq 0.12$, while $T^\star$ rises monotonically with decreasing p (Figs. 18 and 19).

In other cuprates, the location of p_2^{CDW} and $p^\star$ is still not fully established. In Bi-2212, STM studies at $T \simeq 10$ K (below T_c) detect CDW modulations up to $p = 0.17$ and a transition from Fermi arcs (with pseudogap) at $p = 0.17$ to a complete large Fermi surface (without pseudogap) at $p = 0.20$ [18]. In other words, $p_2^{CDW} \simeq p^\star = 0.185 \pm 0.015$. However, normal-state measurements of the pseudogap (above T_c), such as ARPES and Raman, find $p^\star = 0.22 \pm 0.01$ [15,19]. Given this uncertainty, it seems possible that $p^\star \simeq p_2^{CDW} + 0.03$, much as in YBCO and LSCO (Table I).

We infer that CDW ordering is a secondary instability of the pseudogap phase. Two open questions are why it tends to peak at $p \simeq 0.12$ and why its onset at $T = 0$ is delayed relative to $p^\star$.

3. Nematicity

In orthorhombic YBCO, the in-plane resistivity is anisotropic because the CuO chains that run along the b axis conduct. But in addition to this chain-related anisotropy, another anisotropy emerges upon cooling at low doping [73]. The onset of this additional anisotropy, which we will call nematicity, is at a temperature T_{nem} that runs parallel to $T^\star$, some 100 K below (Fig. 18). T_{nem} coincides with the inflexion point in $\rho_a(T)$ [74], i.e., the white line that separates the red and blue regions in the curvature map of Fig. 6. Not surprisingly, this anisotropy is also detected in the Nernst coefficient [74].

Close to the T_{nem} line in the phase diagram at low doping, an anisotropy develops in the spin fluctuation spectrum, detected by inelastic neutron scattering as a splitting in the peak at $Q = (\pi,\pi)$ that appears for one direction and not the other [72]. This “spin nematicity” may be responsible for the transport anisotropy below T_{nem}.

Similarly, a “charge nematicity” is observed in the region of CDW order, at higher doping [74]. Here, the onset of nematicity occurs at $T \simeq T^\star$ [20]. In other words, at temperatures above the SDW and CDW orders, there is a region of enhanced nematic susceptibility, possibly associated with the precursor fluctuations of these two orders [108].

There are three problems with equating this nematic phase with the pseudogap phase. The first is that $T_{nem} < T^\star$ at $p < 0.11$. The second is that nematic order does not open a

TABLE I. Critical dopings for the four cuprate materials discussed in this paper, measured at low temperature ($T \to 0$). The pseudogap critical point $p^\star$ and the beginning and end of the CDW region, at $p_1^{\rm CDW}$ and $p_2^{\rm CDW}$, respectively, were measured in the normal state, reached by suppressing superconductivity with a large magnetic field. The end of the SDW phase, at $p_{\rm SDW}$, is given here for zero field. The doping $p_{\rm FS}$ at which the van Hove singularity occurs is determined by ARPES. It is the doping where the large holelike Fermi surface of overdoped cuprates undergoes a (Lifshitz) transition to a large electronlike Fermi surface upon increasing p. All single numbers with two (three) significant digits have an error bar ± 0.01 (± 0.005). When a doping interval is given, the critical doping is located inside that interval. Information on how the critical dopings were defined can be found in the associated references.

Material	$p^\star$	$p_{\rm FS}$	$p_{\rm SDW}$	$p_1^{\rm CDW}$	$p_2^{\rm CDW}$
YBCO	0.195 [6]	?	0.07 [72]	0.08 [71]	0.16 [6]
LSCO	0.18 [11]	0.17–0.22 [60,90]	0.13 [65,81]	0.085 [80]	0.15 [80]
Nd-LSCO	0.23 [3]	0.20–0.24 [5]	0.24 [51]	?	0.15–0.20 [50]
Eu-LSCO	0.24 [91]	?	?	0.09 [91]	0.16–0.21 [91]

gap (or a pseudogap). The third is that nematic order does not cause a change in carrier density, and so cannot explain the main signature of $p^\star$. But again, nematicity may well be a secondary instability of the pseudogap phase. Or the pseudogap may cause an enhanced nematic susceptibility [109].

4. Intra-unit-cell magnetic order

In the cuprates YBCO, Hg-1201 and Bi-2212, magnetic order has been detected by polarized neutron diffraction, with an onset temperature $T_{\rm mag}$ that coincides roughly with $T^\star$. This intra-unit-cell (IUC) order has a wave vector $Q = 0$. In Fig. 18, we reproduce the reported values of $T_{\rm mag}$ for YBCO [75–77]. We see that in the range $0.09 \leqslant p \leqslant 0.15$, $T_{\rm mag} = T^\star$, within error bars. However, at lower doping ($p \simeq 0.08$), the IUC signal weakens and it onsets at a significantly lower temperature: $T_{\rm mag} = 170 \pm 20$ K [76], while $T^\star = 280 \pm 20$ K (Figs. 3 and 4). It has been suggested that the weakening of the IUC magnetic order in YBCO at low p may be due to a competition with SDW order (or correlations) that develops below the CDW phase, i.e., at $p < p_1^{\rm CDW} = 0.08$. However, the pseudogap does not weaken at $p < p_1^{\rm CDW}$. Indeed, $T^\star$ is higher in our sample with $p = 0.078$, clearly below the CDW region (i.e., with a positive Hall coefficient at low T) [71], than it is in our sample with $p = 0.085$, a doping above $p_1^{\rm CDW}$ (Fig. 4).

A similar discrepancy is observed in LSCO at $p = 0.085$, where $T_{\rm mag} = 120 \pm 20$ K, while $T^\star = 185 \pm 20$ K (Fig. 19). This weakening at low p suggests that the IUC magnetic order is more likely to be a secondary instability of the pseudogap phase, rather than its primary cause. Note that as in the case of nematic order, another $Q = 0$ order, it is difficult to see how the IUC order can open a gap (or a pseudogap) and cause a change in carrier density across $p^\star$.

C. Superconductivity

Unlike the four phases discussed previously, which are all confined to the left of $p^\star$ (and below $T^\star$), the superconducting phase extends beyond the pseudogap critical point. The region of superconductivity in the phase diagram of cuprates is always a dome, which starts at $p_{\rm c1}$ and ends at $p_{\rm c2}$, at low and high doping, respectively. This dome straddles $p^\star$, i.e., $p_{\rm c1} < p^\star$ and $p_{\rm c2} > p^\star$, as we saw for YBCO, LSCO, and Nd-LSCO (Fig. 17). The precise value of $p_{\rm c2}$ may depend on the material, as does the precise value of $p^\star$; in LSCO and Nd-LSCO, $p_{\rm c2} \simeq 0.27$, while $p_{\rm c2} \simeq 0.31$ in Tl-2201 [110] and $p_{\rm c2} \simeq 0.43$ in Bi-2201 [111].

Coming from high p, superconductivity with an order parameter of $d_{x^2-y^2}$ symmetry emerges out of a Fermi-liquid-like metallic state, characterized by a single large coherent holelike Fermi surface [112], with no pseudogap and no broken symmetry of any kind. The big question is: What electron-electron interaction in this simple-looking state causes the electrons to pair? The phase diagrams in Fig. 17 may provide some clues. We already pointed out that a linear extrapolation of the $T^\star(p)$ line reaches $T = 0$ at $p \simeq p_{\rm c2}$, suggesting that the same interactions which favor pairing may also be responsible for the pseudogap.

It turns out that $p_{\rm c2}$ is also the onset of a third manifestation of electron-electron interactions: The appearance of a linear term in the temperature dependence of the resistivity $\rho(T)$, as sketched in Fig. 20. Detailed studies in overdoped Tl-2201 [113–115] and LSCO [10,116] reveal that a linear-T term appears in $\rho(T)$ as soon as $p < p_{\rm c2}$, while $\rho \propto T^2$ at $p > p_{\rm c2}$. This empirical link between linear-T resistivity and $T_{\rm c}$ [117] suggests that the interactions that cause the anomalous inelastic scattering also cause pairing [118]. A similar link has been observed in iron-based and organic superconductors [119], materials whose phase diagrams consist of an antiferromagnetic quantum critical point (QCP) surrounded by a dome of superconductivity. In both cases, the scattering and the pairing are attributed to antiferromagnetic spin fluctuations.

In summary, three fundamental phenomena of cuprates emerge together below $p_{\rm c2}$: superconductivity, pseudogap, and anomalous scattering. (Strictly speaking, the pseudogap opens slightly below $p_{\rm c2}$, at $p^\star$, but in some cases, such as Nd-LSCO and Bi-2201, the separation is small: $p^\star = 0.23$ vs $p_{\rm c2} \simeq 0.27$ [2], and $p^\star = 0.38$ vs $p_{\rm c2} \simeq 0.43$ [17,111], respectively.) Figure 20 suggests another way to summarize the situation. The two fundamental phases of cuprates—superconductivity and pseudogap—are both instabilities of a normal state that is characterized by a linear-T resistivity. Given that a linear-T resistivity is generally observed on the border of antiferromagnetic order and attributed to scattering by antiferromagnetic spin fluctuations, it is tempting to associate both the pseudogap and the d-wave superconductivity in cuprates to antiferromagnetic correlations (perhaps short-ranged). In this scenario, the fact that $T_{\rm c}$ falls at low p while $T^\star$ continues to rise (Fig. 17) is attributed to the competition suffered by the superconducting phase from the full sequence of other phases (Figs. 18 and 19):

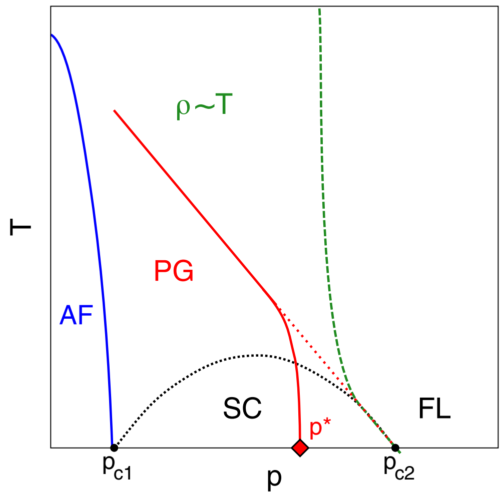

FIG. 20. Schematic phase diagram of cuprates, showing the antiferromagnetic phase (AF, below the blue line), the pseudogap phase (PG, below the red line), and the superconducting dome between p_{c1} and p_{c2} (SC, below the black dotted line). As in Fig. 17, a linear extension of the $T^\star$ line (red) extrapolates to zero at p_{c2}. In the region between the solid red line and the dashed green line, the normal-state resistivity $\rho(T)$ of cuprates is predominantly linear in temperature. This linearity appears below p_{c2}, along with the superconductivity (see text). At $T \to 0$, it persists down to $p^\star$. Above p_{c2}, $\rho \propto T^2$ at low T, the signature of a Fermi-liquid-like metallic state (FL). The green dashed line is drawn to capture the behavior of the linearity of resistivity as observed in LSCO in Fig. 3 of Ref. [10] (the so-called "red foot" contour plot).

first, the pseudogap phase below $p^\star$, then the CDW, SDW, and AF orders below p_2^{CDW}, p_{SDW}, and p_{N}, respectively.

VII. SUMMARY

We have shown how the quasiparticle and superconducting contributions to the Nernst effect in cuprates can be disentangled. We observe that the latter contribution is only significant in a narrow region of temperature above T_c, which extends up to roughly 1.5 T_c, much as the region of paraconductivity observed in the resistivity. We showed how the quasiparticle Nernst signal can be used to detect the onset of the pseudogap phase, at a temperature T_ν. In YBCO, LSCO, and Nd-LSCO, we find that $T_\nu = T_\rho$, the temperature below which the resistivity deviates from its linear-T dependence at high temperature, a standard signature of the pseudogap temperature $T^\star$, consistent with ARPES measurements of the pseudogap. The advantage of using Nernst over resistivity is its much greater sensitivity to $T^\star$. By comparing Nernst data in three La_2CuO_4-based cuprates (LSCO, Nd-LSCO, and Eu-LSCO), we find that they have the same $T^\star(p)$ line (up to $p \simeq 0.17$), independent of their different structures and structural transitions.

We arrive at the temperature-doping phase diagram of two major families of cuprates, YBCO and LSCO, which reveal some qualitative similarities and quantitative differences. Qualitatively, $T^\star(p)$ decreases monotonically with p in both families, along a line that stretches between T_{N} at $p = 0$, where T_{N} is the Néel temperature for the onset of long-range commensurate antiferromagnetic order in the Mott insulator, and p_{c2} at $T = 0$, where p_{c2} is the end point of the superconducting dome at high doping. These empirical links suggest that the pseudogap phase is related to antiferromagnetism and that pseudogap and pairing arise from the same interactions.

Quantitatively, we find that $T^\star(p)$ is 1.5 times larger in YBCO than in LSCO, as is $T_{\mathrm{N}}(0)$. We also find that although $T^\star$ is the same in LSCO and Nd-LSCO, the critical doping at which the pseudogap phase ends abruptly is much lower in LSCO, where $p^\star \simeq 0.18$, than in Nd-LSCO, where $p^\star = 0.23$. A possible explanation for this significant difference is the constraint that the pseudogap can only open once the Fermi surface has undergone its Lifshitz transition through the van Hove singularity, from a large electronlike surface above p_{FS} to a large holelike surface below p_{FS}, i.e., the constraint that $p^\star \leqslant p_{\mathrm{FS}}$.

We briefly discussed four phases that occur inside the pseudogap phase, namely spin density wave (SDW), charge density wave (CDW), nematicity, and intra-unit-cell magnetic order. We conclude that all four are likely to be secondary instabilities of the pseudogap phase, as opposed to its driving mechanism or origin.

Finally, we show that the three primary phenomena of cuprates—the pseudogap, the d-wave superconductivity, and the anomalous metallic behavior (linear-T resistivity)—are found to all emerge together, below p_{c2}. In analogy with other families of materials—such as iron-based, heavy-fermion, and organic superconductors—where linear-T resistivity and superconductivity are observed on the border of antiferromagnetism, we suggest that antiferromagnetic spin fluctuations/correlations may play a common underlying role in these three phenomena.

ACKNOWLEDGMENTS

We thank D. Sénéchal and A.-M. Tremblay for useful discussions and J. Corbin for his assistance with the experiments. L.T. thanks ESPCI-ParisTech, Université Paris-Sud, CEA-Saclay, and the Collège de France for their hospitality and support, and the European Research Council (Grant No. ERC-319286 QMAC) and LABEX PALM (ANR-10-LABX-0039-PALM) for their support, while this paper was written. O.C.C. was supported by a fellowship from the Natural Sciences and Engineering Research Council of Canada (NSERC). J.C. was supported by a fellowship from the Swiss National Science foundation. J.-S.Z. and J.B.G. were supported by a US National Science Foundation grant. H.T. acknowledges MEXT Japan for a Grant-in-Aid for Scientific Research. R.L., D.A.B., and W.N.H. acknowledge funding from the Natural Sciences and Engineering Research Council of Canada (NSERC). L.T. acknowledges support from the Canadian Institute for Advanced Research (CIFAR) and funding from the Natural Sciences and Engineering Research Council of Canada (NSERC; PIN:123817), the Fonds de recherche du Québec - Nature et Technologies (FRQNT), the Canada Foundation for Innovation (CFI), and a Canada Research Chair. Part of this work was funded by the Gordon and Betty Moore Foundation's EPiQS Initiative (Grant No. GBMF5306 to L.T.).

APPENDIX: NERNST SIGNAL FROM SUPERCONDUCTING FLUCTUATIONS

In this paper, our main focus is on the quasiparticle Nernst signal and how it can be used to detect the onset of the pseudogap phase. We only discussed briefly how that signal can be disentangled from the superconducting Nernst signal. In this Appendix, we provide further information on the superconducting Nernst signal in cuprates. We focus on the field dependence of ν as a way to isolate ν_{qp} in YBCO and LSCO. We end by analyzing how prior interpretations of the Nernst effect in cuprates led to the mistaken notion that essentially all the Nernst signal above T_c is due to superconducting fluctuations.

1. Gaussian fluctuations

Recent Nernst measurements in the electron-doped cuprate PCCO have been used to show that a Gaussian theory of superconducting fluctuations can account qualitatively and quantitatively for the observed superconducting signal N_{sc} [120]. Because H_{c2} is very small in PCCO (at most 10 T), one can fully suppress superconducting fluctuations by applying a field $H \simeq 15$ T. This enables one to directly obtain N_{qp}, which can then be subtracted from N to get N_{sc}, and compare this N_{sc} to theory [121–123].

The authors find no difference in the nature of the superconducting fluctuations on the underdoped side of the T_c dome relative to the overdoped side [120]. This shows that the decrease of T_c at low doping is not due to a growth of phase fluctuations, as originally proposed [124]. Rather, the drop in T_c below optimal doping is associated with the critical point where the Fermi surface of PCCO undergoes a reconstruction [125].

A similar study was performed in the hole-doped cuprate Eu-LSCO, in the underdoped regime [28]. The Nernst signal N_{sc} is here also found to agree with Gaussian theory, as in more conventional superconductors, such as NbSi [126]. We note, however, that spectroscopic studies of ARPES [127,128] and STM [129,130] (see Appendix 3 d) show a superconducting gap persisting well above T_c—a fact that is hard to reconcile with Gaussian (amplitude) fluctuations.

The quantitative question of how far in temperature (or in magnetic field) superconducting fluctuations extend above T_c (or above H_{c2}) is in some sense meaningless, for it clearly depends on the sensitivity of the probe. In NbSi, for example, a superconducting Nernst signal was detected up to $30T_c$ and $5H_{c2}$ [126]. Nevertheless, because the extent of the fluctuation regime in cuprate superconductors has been the subject of much debate, we further explore that question in the following sections. We emphasize that in this paper no assumption is made about the nature of the SC fluctuations above T_c nor is any use made of Gaussian theory. Readers interested in learning whether Gaussian theory can describe the superconducting fluctuations measured in cuprates are referred to Refs. [120] and [28].

2. Field dependence and T_B

In YBCO, the separation of quasiparticle and superconducting contributions is straightforward because the former is negative (below $T^\star$) and the latter is positive. In Fig. 2, the minimum in ν/T vs T at T_{min} provides an immediate measure of the temperature below which the superconducting signal becomes important. A plot of T_{min} vs p on the phase diagram reveals that the region of significant superconducting fluctuations closely tracks T_c, with $T_{min} \simeq 1.4T_c$ (Fig. 3). The same conclusion is reached by looking at the paraconductivity in the resistivity, as seen in the curvature map of Fig. 6. This proves the essential point that the pseudogap phase is not a phase of precursor superconductivity. There is no evidence from Nernst data that short-lived Cooper pairs start to form at $T^\star$.

The limitation is that T_{min} cannot be defined for a cuprate with $\nu_{qp} > 0$, like LSCO. We therefore turn to another, more general criterion, based on the field dependence of ν. Indeed, because ν_{sc} always decreases with increasing H, we can say that when ν is independent of field, then ν_{sc} is negligible compared to ν_{qp}. We define T_B to be the temperature above which ν no longer decreases with H.

a. YBCO

Figure 21 shows ν/T vs H for YBCO at doping $p = 0.12$ at different temperatures above $T_c(0) = 66$ K. Note that the value of ν/T at the maximum field (15 T) is subtracted from the isotherms to remove most of the quasiparticle contribution. Let us first examine the a-axis data [panel (a)]. For $T < 90$ K, the field is seen to suppress ν, as expected. For $T > 90$ K, however, there is negligible field dependence. Using the lack of a detectable field dependence to define T_B, we get $T_B = 95 \pm 5$ K, in agreement with $T_{min} = 90 \pm 5$ K in that sample (Fig. 3).

In panel (b) of Fig. 21, we show the b-axis isotherms in YBCO at $p = 0.12$. At $T = 70$ K (pale blue curve) and $T = 75$ K (black curve), we see clearly that the field suppresses the superconducting signal. But it also causes a positive rise in ν, thereby producing a minimum in ν vs H.

We attribute this positive "magnetoresistance," which grows as H^2 (or as H^3 if plotted as N vs H), to the quasiparticle component of the Nernst signal [120]. [All odd (even) powers of H are allowed by symmetry in $N(\nu)$.] The H^2 dependence is best seen at $T = 90$ K (green curve), where ν/T vs H is perfectly described by a quadratic fit (dashed line in Fig. 21). (It is possible that the same H^2 contribution is in fact present in the a-axis data, but with a much reduced magnitude, perhaps in proportion with the ten-time smaller quasiparticle signal [20].) At low H, a superconducting signal is seen above the H^2 background (dashed line) at $T = 80$ K, for example. For the b-axis isotherms, we define T_B to be the temperature above which $\nu(H)$ is purely quadratic, giving $T_B = 90 \pm 5$ K for this doping, in agreement, within error bars, with the value obtained from the a-axis isotherms.

In summary, we find that $T_{min} \simeq T_B = (1.4 \pm 0.05)\, T_c$ at $p = 0.12$, as also found at other nearby dopings (Fig. 3). Note that this is consistent with the onset of paraconductivity in the DC resistivity (Fig. 6) and microwave conductivity (see Appendix 3 c).

b. LSCO

In order to delineate the region of significant superconducting fluctuations in LSCO, we can use paraconductivity, as was done for YBCO. In Fig. 16, we see that the onset of paraconductivity in LSCO occurs at a temperature T_{para} between 50 K and 65 K, in the range $0.08 < p < 0.20$ [12].

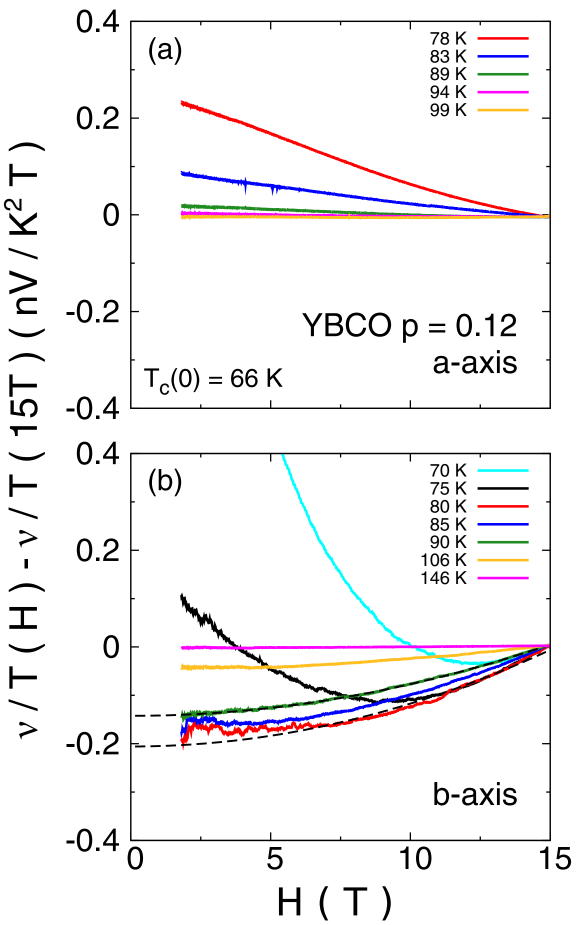

FIG. 21. Nernst coefficient of YBCO at doping $p = 0.12$ with thermal gradient applied along the a axis [panel (a)] and b axis [panel (b)], plotted as $\nu/T(H) - \nu/T$ (15 T), versus magnetic field, at various temperatures as indicated. In (a), the isotherms above $T_c(0) =$ 66 K show a field-induced suppression, for $T < T_B = 95 \pm 5$ K. Above T_B, the field dependence of ν is negligible. We use T_B as a second criterion to define the onset of superconducting fluctuations, in addition to T_{min}. In (b), isotherms immediately above $T_c(0)$ (70 K and 75 K) also show a field-induced suppression of the superconducting signal. Isotherms far above T_c (90 K and 106 K) show a field-induced growth of $\nu(H)$, proportional to H^2 (dashed lines), due to a "magnetoresistance" in the quasiparticle contribution to the Nernst signal (see text). At low H, a superconducting signal is seen above the H^2 background (dashed line) at $T = 80$ K, for example. The temperature above which $\nu(H)$ is purely quadratic is $T_B = 90 \pm 5$ K.

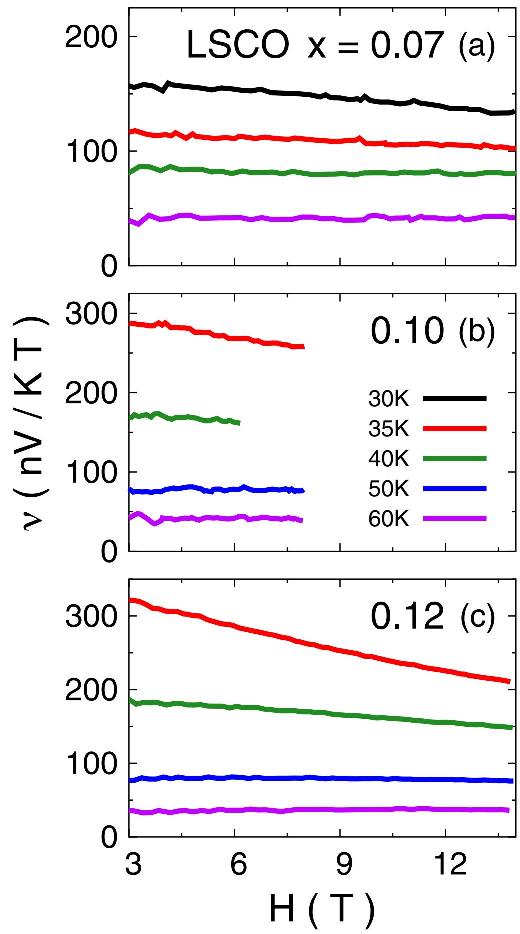

FIG. 22. Field dependence of the Nernst coefficient in LSCO at doping $x = p = 0.07$ [(a); $T_c = 11$ K], 0.10 [(b); $T_c = 28$ K], and 0.12 [(c); $T_c = 29$ K] at various temperatures above T_c (color-coded legend). These curves show that above a certain temperature, defined as T_B, the Nernst coefficient ($\nu \equiv N/H$) is essentially field independent. The strong field dependence associated with superconducting fluctuations gone, the quasiparticle field-independent contribution dominates the signal. We find $T_B = 40 \pm 10$, 50 ± 10, and 50 ± 10 K for $x = 0.07$, 0.10, and 0.12, respectively. These T_B values are plotted on the curvature map of Fig. 16 and are seen to fall on the boundary of the paraconductivity region. Data at $p = 0.07$ and 0.12 are taken from Ref. [27], at $p = 0.10$ from Ref. [43].

(Note that the weak p dependence of T_{para} may come from some inhomogeneity in doping, whereby parts of all samples have some optimally-doped regions, where T_c is highest.) At optimal doping, where $T_c = 40$ K, $T_{para} \simeq 65$ K, so that $T_{para} \simeq 1.6 T_c$.

It is harder to disentangle superconducting and quasiparticle contributions to the Nernst signal in LSCO-based materials because unlike YBCO the quasiparticle contribution also rises positively with decreasing temperature, so there is no equivalent of T_{min}. We therefore use the lack of a detectable field dependence to define T_B, as our criterion for the onset of superconducting fluctuations. Figure 22 shows ν as a function of magnetic field H for LSCO at three dopings (0.07, 0.10, and 0.12), at $T > T_c$. We can extract T_B from these curves as the temperature above which the isotherms are flat: $T_B = 40 \pm 10$, 50 ± 10, and 50 ± 10 K for $x = 0.07$, 0.10, and 0.12, respectively. We note that the available data is limited to $\approx$10 T and it would be interesting to see if this flatness can be tracked at higher fields. T_B is then plotted as a function of doping on the curvature map of LSCO (Fig. 16). It is seen to fall more or less on the boundary of the paraconductivity region (blue band above T_c), i.e., $T_B \simeq T_{para}$.

c. Comparing LSCO to Nd-LSCO

Another approach for disentangling ν_{sc} and ν_{qp} in LSCO is to compare with Nd-LSCO, its lower-T_c counterpart, at the same doping. As seen in Fig. 23(a), at high temperature $\nu(T)$ is essentially identical in LSCO and Nd-LSCO, and it is not due to superconducting fluctuations. Therefore, comparing

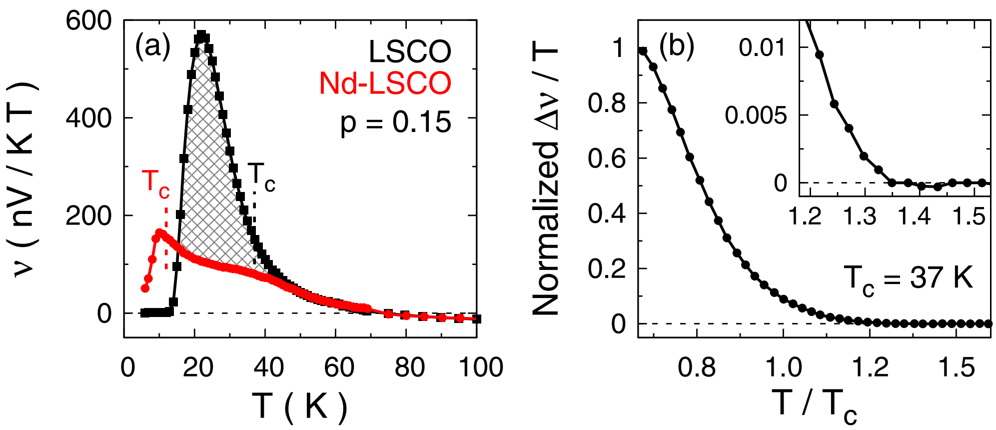

FIG. 23. (a) Nernst coefficient ν of Nd-LSCO (red circles) and LSCO (black squares) at $p = 0.15$ versus temperature, measured with $H = 9$ T (data from Ref. [44]). At high T, there is good agreement between the two data sets (see also Fig. 9), until the superconducting fluctuations in LSCO start to grow, below ~50 K. This difference (cross-hatched region) is attributable to their different T_c (37 K for LSCO and 12 K for Nd-LSCO) and can be seen as the superconducting fluctuations contribution for LSCO. (b) Difference between ν of LSCO and Nd-LSCO [cross-hatched region of panel (a)], plotted as $\Delta\nu/T$, normalized at maximum value, versus normalized temperature T/T_c (where T_c is the T_c of LSCO). Subtracting Nd-LSCO from LSCO has the effect of taking away the quasiparticle contribution and revealing the superconducting contribution to the Nernst signal in LSCO. This superconducting contribution is seen to decrease rapidly with increasing temperature, vanishing around $1.35T_c$ (see inset).

the two materials should reveal the onset of a detectable superconducting contribution in LSCO, since its T_c is higher than in Nd-LSCO. Figure 23(a) compares LSCO and Nd-LSCO at $p = 0.15$, using data from Ref. [44], where $T_c = 37$ K and 12 K, respectively. Down to 50 K or so, the data are nearly identical, even through the LTT structural transition of Nd-LSCO (at 70 K). Below 50 K, the two curves deviate, with the LSCO curve showing a pronounced superconducting peak. This difference between the two curves [shaded region in Fig. 23(a)] can be viewed as the superconducting contribution of LSCO. Figure 23(b) plots the difference $\Delta\nu$ between the two data sets (normalized at maximum value) vs T/T_c, with $T_c =$ 37 K (in LSCO). In the inset, a zoom shows that the difference becomes nonzero below ~$1.4T_c$. This puts a reasonable upper bound on a detectable superconducting Nernst signal in LSCO. We conclude that the regime of significant superconducting fluctuations in LSCO extends up to $1.5 \pm 0.1T_c$, with the error bar covering the various criteria (paraconductivity in the resistivity, field independence in the Nernst signal, comparison to Nd-LSCO).

3. Other probes and materials

a. Nernst effect in Bi-2201 and Hg-1201

In this paper on the Nernst effect in cuprates, we have focused on YBCO and LSCO (as well as Nd-LSCO and Eu-LSCO). Now, studies of the Nernst effect have also been carried out on other cuprates, such as Bi-2212 and Bi-2201. They lead to the same basic finding that the regime of SC fluctuations tracks T_c and ends well below the pseudogap temperature $T^\star$. In Fig. 24, we plot the temperature $T^{\rm onset}$ below which the Nernst signal in Bi-2201 becomes detectable in the data of Ref. [131]. Note that $T^{\rm onset}$ is necessarily an upper bound on the regime of SC fluctuations. Looking closely at the data across the doping range, one finds no trace of any signal above 70 K. As discussed below (Appendix 3 b), this value is consistent with the upper limit on detectable SC fluctuations in torque magnetometry data on Bi-2201. What is clear from Fig. 24 is that $T^{\rm onset}$ in Bi-2201 is flat vs doping, with $T^{\rm onset} \simeq$ 65 K across the phase diagram, whereas $T^\star$ rises with underdoping, to values as high as $T^\star \simeq 250$ K at low doping. This is therefore very similar to the phase diagram of LSCO shown in Fig. 26. Both LSCO and Bi-2201 lead us to the same conclusion as reached for YBCO: The regime of SC fluctuations tracks T_c, and it lies well below the pseudogap temperature $T^\star$.

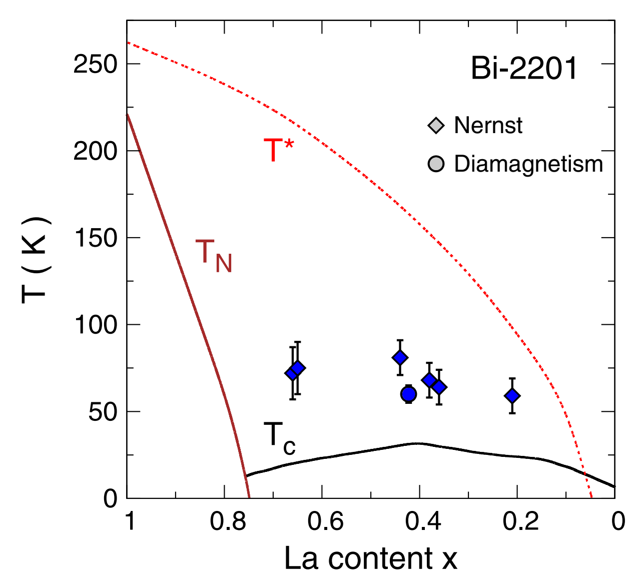

FIG. 24. Temperature-doping phase diagram of Bi-2201 as a function of La doping x, showing T_N (brown line), T_c (black line), and $T^\star$ detected by NMR (dashed red line) (from Ref. [17]). Blue diamonds mark the onset of a finite Nernst signal ($T^{\rm onset}$; Ref. [131]), attributed to SC fluctuations. Also shown is the onset temperature for SC fluctuations in Bi-2201 detected by torque magnetometry near optimal doping (blue circle; Refs. [132,133]).

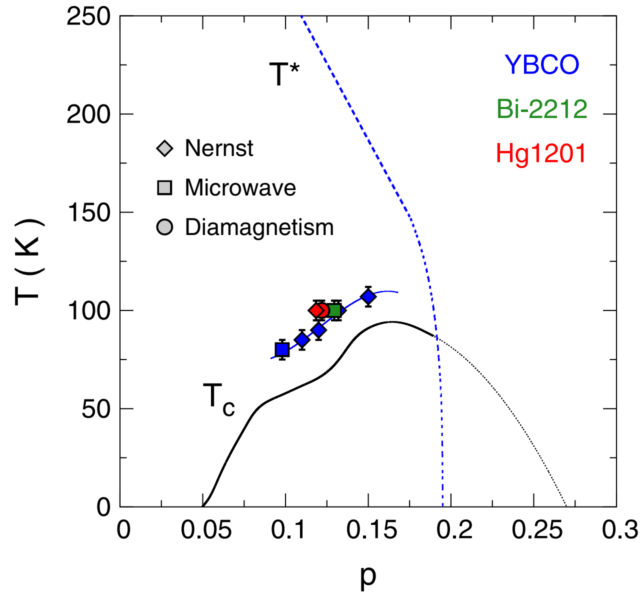

FIG. 25. Temperature-doping phase diagram of YBCO, showing the pseudogap temperature $T^\star$ (dashed blue line) and the onset of SC fluctuations detected in the Nernst signal ($T_{\rm min}$, blue diamonds; from Fig. 3) and in the microwave conductivity (blue square; from Ref. [135]). In addition, the onset temperature for SC fluctuations in Bi-2212 (green) and Hg-1201 (red) is also displayed, for samples with a T_c value given by the solid black line, from Nernst (red diamond, $T_{\rm min}$; Ref. [21]), microwave (green square; Ref. [134]) and magnetization (red circle; Refs. [132,133]) data. Three different measurements on three different cuprates are seen to yield a very similar regime of SC fluctuations, close to T_c and well below $T^\star$.

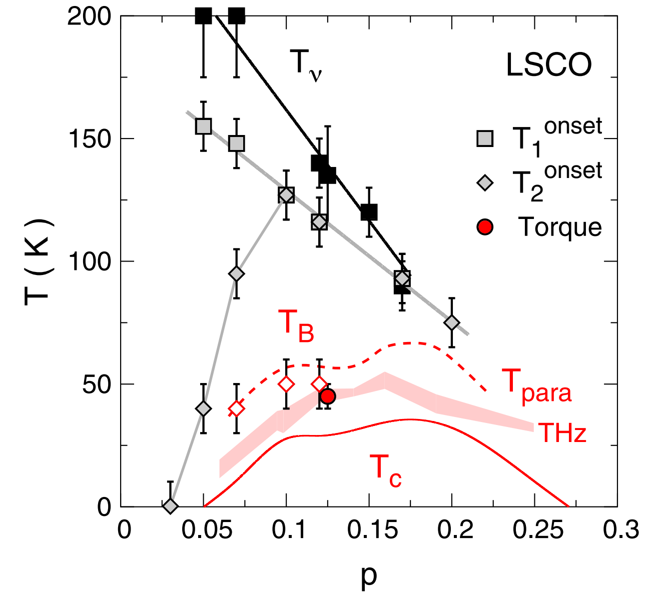

FIG. 26. Temperature-doping phase diagram of LSCO from the Princeton group (gray). The early version of their phase diagram [43] plots an onset temperature, labeled $T_1^{\rm onset}$ (gray squares), defined as the temperature below which $\nu(T)$ starts to rise upon cooling. In a later version of their phase diagram [27,45], they plot a revised onset temperature, which we label $T_2^{\rm onset}$ (gray diamonds). For $p \geqslant 0.10$, $T_2^{\rm onset} \equiv T_1^{\rm onset}$; for $p < 0.10$, $T_2^{\rm onset}$ is the temperature below which $\nu{+}\mu S$ starts to rise upon cooling, where μ is the mobility and S the Seebeck coefficient (see text). For comparison, we also plot the T_ν values reported here for LSCO (black squares, Fig. 10), i.e., the pseudogap temperature $T^\star$ defined as the deviation from linearity in ν/T vs T (Fig. 15). In red, we show the various signatures of superconductivity: T_c (solid line); T_B (open diamonds, Fig. 16); $T_{\rm para}$, the onset of paraconductivity (dashed line, Fig. 16); the onset of superconducting fluctuations probed by terahertz spectroscopy (pink shading [137]) and by torque magnetization (red circle [132,133]).

As for YBCO, Nernst measurements on Hg-1201 have the advantage of a negative quasiparticle signal, so that the onset of SC fluctuations can immediately be detected as a minimum occurring at $T_{\rm min}$. For a sample with $T_c = 65$ K, $T_{\rm min} = 100 \pm 5$ K [21]. In Fig. 25, we show how this compares to the $T_{\rm min}$ values in YBCO, where for the same T_c one gets $T_{\rm min} = 90 \pm 5$ K (Fig. 3).

b. Torque magnetometry

In this paper, we have seen that the resistivity and the Nernst coefficient can both be used to detect the onset of SC fluctuations above T_c. Magnetization is another probe of such fluctuations, and torque magnetometry measurements have been carried out on several cuprates. Detailed high-sensitivity torque measurements of three different cuprates [132,133] reveal that SC fluctuations can no longer be detected above $T = 45 \pm 5$ K in LSCO at $p = 0.125$ (in good agreement with $T_B = 50 \pm 10$ K; see Fig. 26), $T = 60 \pm 5$ K in Bi-2201 at optimal doping (in good agreement with $T^{\rm onset} \simeq 65$ K; see Fig. 24), and $T = 100 \pm 5$ K in underdoped Hg-1201 (in good agreement with $T_{\rm min} = 100$ K; see Fig. 25).

c. Microwave and THz conductivity

SC fluctuations can also be detected via measurements at microwave and THz frequencies. In a seminal study using microwave measurements, Corson and co-workers detected SC fluctuations in an underdoped sample of Bi-2212 with $T_c = 74$ K up to at most $T = 100$ K [134]. As shown in Fig. 25, this upper limit for the fluctuation regime in Bi-2212 agrees perfectly with $T_{\rm min} = 100 \pm 10$ K measured in YBCO for the same value of T_c. More recent microwave measurements on YBCO itself [135] confirm the excellent agreement with $T_{\rm min}$ (Fig. 25). Measurements on LSCO at THz frequencies find that the regime of SC fluctuations tracks T_c closely, as displayed in Fig. 26, in excellent agreement with the torque magnetization and with T_B from the Nernst effect.

d. ARPES and STM

Although some ARPES studies (e.g., Ref. [136]) find that the superconducting gap closes at T_c, other studies find a superconducting gap persisting above T_c. For example, Reber and co-workers argue that in underdoped Bi-2212 such a gap extrapolates to zero only at $T = 1.4\ T_c$ [127], an observation confirmed by a recent high-resolution laser-ARPES study [128]. This is roughly consistent with the microwave data mentioned in the previous section.

STM studies on Bi-2212 also find superconductivity persisting above T_c [129], in one case [130] up to temperatures much higher than the limit imposed by the ARPES and microwave data.

4. The Princeton interpretation

Following the seminal work of the Princeton group in the period 2000–2006 [27,41,43,45,138,139], the Nernst effect in cuprates has been widely attributed to superconducting fluctuations, and in the underdoped regime those have been mostly interpreted as *phase* fluctuations, detectable in some cases up to $\sim 5T_c$. This has been viewed as evidence that short-lived Cooper pairs without phase coherence form at temperatures well above T_c. In this paper, we have argued that the superconducting Nernst signal does not, in fact, extend very far above T_c, becoming negligible above $\sim 1.5T_c$. Moreover, recent studies suggest that even in the underdoped regime these fluctuations are not *phase* fluctuations, but rather Gaussian fluctuations of both the amplitude and the phase of the order parameter [28,120]. (Phase fluctuations may appear at very low doping.)

In this section, we examine the analysis performed by the Princeton group to understand why their interpretation is different from our own. We emphasize that the data themselves are perfectly consistent amongst the various groups, so that the disagreement is on the analysis and interpretation only. This discussion will focus on LSCO data.

A first difference in the analysis lies in the definition of the onset temperature. The Princeton group defines the onset of the low-temperature rise in the Nernst signal of LSCO (and other cuprates) as the temperature T^{onset} below which $\nu(T)$ (rather than $\nu(T)/T$) starts to rise upon cooling. In general, this T^{onset} is not equal to our T_ν (defined as the temperature below which ν/T starts to rise). For example, data on LSCO at $p = 0.15$, plotted as ν vs T in Fig. 23(a), yield $T^{\text{onset}} \simeq 100$ K, while we get $T_\nu = 120 \pm 10$ K from the same data plotted as ν/T vs T (Fig. 13).

As shown in Fig. 26, a plot of T^{onset} vs p (T_1^{onset}, open squares [43]) yields a line that is qualitatively similar to the T_ν line in Fig. 10 (full squares in Fig. 26), but slightly lower. Although the difference is not huge, it is nevertheless significant, and adopting the correct definition is important to arrive at a meaningful onset temperature.

For the same reason that one should plot C/T, κ/T, and S/T when analyzing the specific heat C, thermal conductivity κ, and thermopower S of a metal, one should plot ν/T rather than ν when analyzing the Nernst coefficient [see Eq. (2)]. Because the laws of thermodynamics require that all four quantities (C, κ, S, and ν) go to zero as $T \to 0$, the negative ν observed at high T in LSCO [Fig. 23(a)] must inevitably rise upon cooling, but this rise may not reflect any change in the electronic behavior. This point is illustrated by the data on Nd-LSCO at $p = 0.24$ (Fig. 11), which show a monotonic decrease of ν/T vs T as $T \to 0$. There is no upturn and so $T_\nu = 0$. The absence of a pseudogap temperature (or any other characteristic temperature) is confirmed by the fact that the resistivity is featureless and perfectly linear below 50 K [Fig. 5(d)]. By contrast, if we were to plot ν vs T instead, we would necessarily obtain $T^{\text{onset}} > 0$, suggesting that there is a meaningful crossover, in contradiction with the featureless $\rho(T)$. Furthermore, the good agreement between T_ν and T_ρ for both YBCO (Fig. 3) and Nd-LSCO (Fig. 10) validates the use of ν/T to define the onset of the change in $\nu(T)$ at high temperature.

Beyond the issue of the correct definition (whether T_ν or T^{onset}), the real question is what causes ν to initially rise upon cooling below T^{onset}? We attribute the initial rise in $\nu(T) = \nu_{\text{qp}}(T) + \nu_{\text{sc}}(T)$ (coming down from high temperature) to a change in the quasiparticle component $\nu_{\text{qp}}(T)$, while the Princeton group attributes this rise to a growth in the superconducting component $\nu_{\text{sc}}(T)$. In 2000, this was their interpretation for all dopings [43], down to $x = 0.05$, their lowest doping (Fig. 26).

In 2001, they realized that this interpretation is incorrect at low doping [45], by examining the behavior of $\nu + \mu S$, where $\mu = \tan\theta_{\text{H}}/H$ is the mobility and S is the Seebeck coefficient. At $x = 0.05$, they recognized that the initial rise in $\nu(T)$ from high temperature, reaching +40 nV/KT at $T = 60$ K is in fact due to an increase in the quasiparticle term $\nu_{\text{qp}}(T)$. Only below 40 K is there an additional rise coming from superconducting fluctuations. They therefore revised the estimated temperature for the onset of superconducting fluctuations from $T_1^{\text{onset}} = 150$ K [43] down to $T_2^{\text{onset}} = 40$ K [45] (see Fig. 26). However, the Princeton group adopted the view that such a revision was only needed for $x < 0.10$, arguing that any rise in $\nu_{\text{qp}}(T)$ is negligible for $x \geqslant 0.10$. This is where we disagree. At $x = 0.10$, $\nu(T)$ also rises up to +40 nV/KT at $T = 60$ K [43], a rise that is very similar to the above-mentioned rise seen at $x = 0.05$. Why, then, would the rise in $\nu(T)$ at $x = 0.10$ not also come from $\nu_{\text{qp}}(T)$? A rough estimate of ν_{qp} can be obtained by looking at μS [23]. The Princeton data show that μS at $T = 60$ K is actually larger at $x = 0.10$, not smaller. Indeed, $\mu S \simeq 90$ nV/KT (Fig. 3(a) in Ref. [43]), while $\mu S \simeq 60$ nV/KT at $x = 0.05$ (Fig. 3(b) in Ref. [45]). Moreover, the measured ν(60K) is comparable, namely $\nu = 40$ nV/KT at both dopings $x = 0.05$ and $x = 0.10$. These numbers show clearly that there is no reason to assume that ν_{qp} can be neglected at $x = 0.10$.

We see that in LSCO, just as in Eu-LSCO [see Fig. 8(c)] and Nd-LSCO (see Fig. 9), the initial rise in $\nu(T)$, below T^{onset}, is in fact due to ν_{qp}, and the rise in ν_{sc} only starts at much lower temperature.

Not surprisingly, the fact of using different criteria for T^{onset} for dopings above and below $p = 0.10$ causes a sharp change in T^{onset} at that doping, producing an artificial peak at $p = 0.10$ (see T_2^{onset}; gray diamonds in Fig. 26). The resulting T^{onset} line has no clear relation to the real onset of superconducting fluctuations. For example, the peak value, at $p = 0.10$, is $T^{\text{onset}} = 125 \pm 10$ K, whereas at that doping the onset of paraconductivity occurs at $T_{\text{para}} \simeq 60$ K (Fig. 16) and the onset of field dependence in $\nu(T)$ occurs at $T_{\text{B}} = 50 \pm 10$ K (Fig. 22). Moreover, the onset of superconducting fluctuations detected in both THz conductivity (Appendix 3 c) and torque magnetization (Appendix 3 b) is 45 ± 5 K (Fig. 26). In summary, the widely used Nernst phase diagram of T_2^{onset} vs p in LSCO (gray diamonds in Fig. 26) does not correspond to the region of superconducting fluctuations in LSCO.

The Princeton group has also used torque magnetometry as a separate way to detect superconducting fluctuations above T_c [140]. They define an onset temperature of diamagnetism (from superconducting fluctuations), $T_{\text{onset}}^{\text{M}}$, as the temperature below which the magnetization (or susceptibility) deviates downwards, towards negative values, from a positive paramagnetic background presumed to have a linear temperature dependence. The values of $T^{\mathrm{M}}_{\mathrm{onset}}$ they extract as a function of doping agree with the T_2^{onset} vs p in Fig. 26. They argue that this reinforces their interpretation of T_2^{onset} as being the onset of superconducting fluctuations above T_c in the phase diagram [140].

The assumption of a linear-in-temperature magnetization background has been questioned [132,133,141]. In particular, it neglects the effect of the pseudogap phase on the paramagnetic susceptibility [141]. (To attribute a downward drop in the susceptibility from its linear-T dependence at high T to diamagnetism is a bit like attributing the downward drop in the resistivity of YBCO from its linear-T dependence at T_ρ [Fig. 5(a)] to paraconductivity.) To properly identify the diamagnetism that comes from superconductivity, Yu and coworkers [132,133] used its nonlinear field dependence (and the emergence of higher harmonics in its angular dependence). This is similar to our definition of T_{B} from the Nernst signal. With this criterion, Yu *et al.* find that superconducting fluctuations are significant (in the magnetization signal) only in a narrow temperature region above the superconducting dome, up to at most $\sim 1.5T_c$, in LSCO, Bi-2201, and Hg-1201 [132,133]. This narrow regime of SC fluctuations, much narrower than that reported by the Princeton group, is consistent with several probes (T_{B} from Nernst, paraconductivity from DC resistivity, microwave, and THz conductivity) applied to several cuprates (YBCO, LSCO, Bi-2201, Bi-2212, Hg-1201), as shown in Figs. 24, 25, and 26.

Note that the field and temperature dependence of the magnetization data by the Princeton group can be explained in terms of a Gaussian Ginzburg-Landau approach [142]. The theory of Gaussian superconducting fluctuations was also shown to provide a valid quantitative description of diamagnetism data in YBCO [143]. We conclude that the scenario of strong phase fluctuations in underdoped cuprates is neither supported by Nernst data nor by magnetization data, except perhaps close to $p = p_{c1} \simeq 0.05$.

5. Summary

To summarize this Appendix, several different measurements and properties, including the Nernst effect, paraconductivity, magnetization, terahertz spectroscopy, and microwave conductivity—applied to a variety of materials, including YBCO, LSCO, Bi-2201, Bi-2212, Hg-1201—point to the same conclusion: Significant superconducting fluctuations are present in cuprates only in a temperature interval close to T_c and well below $T^\star$.

[1] A. Damascelli, Z. Hussain, and Z.-X. Shen, Rev. Mod. Phys. **75**, 473 (2003).

[2] R. Daou, N. Doiron-Leyraud, D. LeBoeuf, S. Y. Li, F. Laliberté, O. Cyr-Choinière, Y. J. Jo, L. Balicas, J.-Q. Yan, J.-S. Zhou, J. B. Goodenough, and L. Taillefer, Nat. Phys. **5**, 31 (2009).

[3] C. Collignon, S. Badoux, S. A. A. Afshar, B. Michon, F. Laliberté, O. Cyr-Choinière, J.-S. Zhou, S. Licciardello, S. Wiedmann, N. Doiron-Leyraud, and L. Taillefer, Phys. Rev. B **95**, 224517 (2017).

[4] O. Cyr-Choinière, R. Daou, J. Chang, F. Laliberté, N. Doiron-Leyraud, D. LeBoeuf, Y. J. Jo, L. Balicas, J.-Q. Yan, J.-G. Cheng, J.-S. Zhou, J. B. Goodenough, and L. Taillefer, Physica C (Amsterdam) **470**, S12 (2010), in Proceedings of the 9th International Conference on Materials and Mechanisms of Superconductivity.

[5] C. E. Matt, C. G. Fatuzzo, Y. Sassa, M. Månsson, S. Fatale, V. Bitetta, X. Shi, S. Pailhès, M. H. Berntsen, T. Kurosawa, M. Oda, N. Momono, O. J. Lipscombe, S. M. Hayden, J.-Q. Yan, J.-S. Zhou, J. B. Goodenough, S. Pyon, T. Takayama, H. Takagi, L. Patthey, A. Bendounan, E. Razzoli, M. Shi, N. C. Plumb, M. Radovic, M. Grioni, J. Mesot, O. Tjernberg, and J. Chang, Phys. Rev. B **92**, 134524 (2015).

[6] S. Badoux, W. Tabis, F. Laliberté, G. Grissonnanche, B. Vignolle, D. Vignolles, J. Béard, D. A. Bonn, W. N. Hardy, R. Liang, N. Doiron-Leyraud, L. Taillefer, and C. Proust, Nature (London) **531**, 210 (2016).

[7] J. Tallon and J. Loram, Physica C (Amsterdam) **349**, 53 (2001).

[8] F. Rullier-Albenque, H. Alloul, and G. Rikken, Phys. Rev. B **84**, 014522 (2011).

[9] G. S. Boebinger, Y. Ando, A. Passner, T. Kimura, M. Okuya, J. Shimoyama, K. Kishio, K. Tamasaku, N. Ichikawa, and S. Uchida, Phys. Rev. Lett. **77**, 5417 (1996).

[10] R. A. Cooper, Y. Wang, B. Vignolle, O. J. Lipscombe, S. M. Hayden, Y. Tanabe, T. Adachi, Y. Koike, M. Nohara, H. Takagi, C. Proust, and N. E. Hussey, Science **323**, 603 (2009).

[11] F. Laliberté, W. Tabis, S. Badoux, B. Vignolle, D. Destraz, N. Momono, T. Kurosawa, K. Yamada, H. Takagi, N. Doiron-Leyraud, C. Proust, and L. Taillefer, arXiv:1606.04491.

[12] Y. Ando, S. Komiya, K. Segawa, S. Ono, and Y. Kurita, Phys. Rev. Lett. **93**, 267001 (2004).

[13] N. E. Hussey, R. A. Cooper, X. Xu, Y. Wang, I. Mouzopoulou, B. Vignolle, and C. Proust, Philos. Trans. R. Soc. London A **369**, 1626 (2011).

[14] T. Kondo, Y. Hamaya, A. D. Palczewski, T. Takeuchi, J. S. Wen, Z. J. Xu, G. Gu, J. Schmalian, and A. Kaminski, Nat. Phys. **7**, 21 (2011).

[15] I. M. Vishik, M. Hashimoto, R.-H. He, W.-S. Lee, F. Schmitt, D. Lu, R. G. Moore, C. Zhang, W. Meevasana, T. Sasagawa, S. Uchida, K. Fujita, S. Ishida, M. Ishikado, Y. Yoshida, H. Eisaki, Z. Hussain, T. P. Devereaux, and Z.-X. Shen, Proc. Natl. Acad. Sci. USA **109**, 18332 (2012).

[16] Y. He, Y. Yin, M. Zech, A. Soumyanarayanan, M. M. Yee, T. Williams, M. C. Boyer, K. Chatterjee, W. D. Wise, I. Zeljkovic, T. Kondo, T. Takeuchi, H. Ikuta, P. Mistark, R. S. Markiewicz, A. Bansil, S. Sachdev, E. W. Hudson, and J. E. Hoffman, Science **344**, 608 (2014).

[17] S. Kawasaki, C. Lin, P. L. Kuhns, A. P. Reyes, and G.-Q. Zheng, Phys. Rev. Lett. **105**, 137002 (2010).

[18] K. Fujita, C. K. Kim, I. Lee, J. Lee, M. H. Hamidian, I. A. Firmo, S. Mukhopadhyay, H. Eisaki, S. Uchida, M. J. Lawler, E.-A. Kim, and J. C. Davis, Science **344**, 612 (2014).

[19] S. Benhabib, A. Sacuto, M. Civelli, I. Paul, M. Cazayous, Y. Gallais, M.-A. Méasson, R. D. Zhong, J. Schneeloch, G. D. Gu, D. Colson, and A. Forget, Phys. Rev. Lett. **114**, 147001 (2015).

[20] R. Daou, J. Chang, D. LeBoeuf, O. Cyr-Choinière, F. Laliberté, N. Doiron-Leyraud, B. J. Ramshaw, R. Liang, D. A. Bonn, W. N. Hardy, and L. Taillefer, Nature (London) **463**, 519 (2010).

[21] N. Doiron-Leyraud, S. Lepault, O. Cyr-Choinière, B. Vignolle, G. Grissonnanche, F. Laliberté, J. Chang, N. Barišić, M. K. Chan, L. Ji, X. Zhao, Y. Li, M. Greven, C. Proust, and L. Taillefer, Phys. Rev. X **3**, 021019 (2013).

[22] N. Doiron-Leyraud, O. Cyr-Choinière, S. Badoux, A. Ataei, C. Collignon, A. Gourgout, S. Dufour-Beauséjour, F. F. Tafti, F. Laliberté, M.-E. Boulanger, M. Matusiak, D. Graf, M. Kim, J.-S. Zhou, N. Momono, T. Kurosawa, H. Takagi, and L. Taillefer, Nat. Commun. **8**, 2044 (2017).

[23] K. Behnia, J. Phys.: Condens. Matter **21**, 113101 (2009).

[24] K. Behnia, *Fundamentals of Thermoelectricity* (Oxford University Press, Oxford, 2015).

[25] K. Behnia and H. Aubin, Rep. Prog. Phys. **79**, 046502 (2016).

[26] R. P. Huebner, *Magnetic Flux Structures in Superconductors* (Springer, Berlin, 1979).

[27] Y. Wang, L. Li, and N. P. Ong, Phys. Rev. B **73**, 024510 (2006).

[28] J. Chang, N. Doiron-Leyraud, O. Cyr-Choinière, G. Grissonnanche, F. Laliberté, E. Hassinger, J.-P. Reid, R. Daou, S. Pyon, T. Takayama, H. Takagi, and L. Taillefer, Nat. Phys. **8**, 751 (2012).

[29] P. Li and R. L. Greene, Phys. Rev. B **76**, 174512 (2007).

[30] O. Cyr-Choinière, R. Daou, F. Laliberté, D. LeBoeuf, N. Doiron-Leyraud, J. Chang, J.-Q. Yan, J.-G. Cheng, J.-S. Zhou, J. B. Goodenough, S. Pyon, T. Takayama, H. Takagi, Y. Tanaka, and L. Taillefer, Nature (London) **458**, 743 (2009).

[31] R. Bel, H. Jin, K. Behnia, J. Flouquet, and P. Lejay, Phys. Rev. B **70**, 220501 (2004).

[32] E. Hassinger, G. Knebel, K. Izawa, P. Lejay, B. Salce, and J. Flouquet, Phys. Rev. B **77**, 115117 (2008).

[33] R. Liang, D. A. Bonn, and W. N. Hardy, Philos. Mag. **92**, 2563 (2012).

[34] R. Liang, D. A. Bonn, and W. N. Hardy, Phys. Rev. B **73**, 180505 (2006).

[35] F. Rullier-Albenque, R. Tourbot, H. Alloul, P. Lejay, D. Colson, and A. Forget, Phys. Rev. Lett. **96**, 067002 (2006).

[36] T. Ito, K. Takenaka, and S. Uchida, Phys. Rev. Lett. **70**, 3995 (1993).

[37] F. Rullier-Albenque, H. Alloul, F. Balakirev, and C. Proust, Europhys. Lett. **81**, 37008 (2008).

[38] S. Ono, Y. Ando, T. Murayama, F. F. Balakirev, J. B. Betts, and G. S. Boebinger, Phys. Rev. Lett. **85**, 638 (2000).

[39] N. Momono, M. Ido, T. Nakano, M. Oda, Y. Okajima, and K. Yamaya, Physica C (Amsterdam) **233**, 395 (1994).

[40] D. Bergeron, V. Hankevych, B. Kyung, and A.-M. S. Tremblay, Phys. Rev. B **84**, 085128 (2011).

[41] N. Ong, Y. Wang, S. Ono, Y. Ando, and S. Uchida, Ann. Phys. **13**, 9 (2004).

[42] G. Sordi, P. Sémon, K. Haule, and A.-M. Tremblay, Sci. Rep. **2**, 547 (2012).

[43] Z. A. Xu, N. P. Ong, Y. Wang, T. Kakeshita, and S. Uchida, Nature (London) **406**, 486 (2000).

[44] T. Fujii, T. Matsushima, T. Maruoka, and A. Asamitsu, Physica C (Amsterdam) **470**, S21 (2010), in Proceedings of the 9th International Conference on Materials and Mechanisms of Superconductivity.

[45] Y. Wang, Z. A. Xu, T. Kakeshita, S. Uchida, S. Ono, Y. Ando, and N. P. Ong, Phys. Rev. B **64**, 224519 (2001).

[46] N. Ichikawa, S. Uchida, J. M. Tranquada, T. Niemöller, P. M. Gehring, S.-H. Lee, and J. R. Schneider, Phys. Rev. Lett. **85**, 1738 (2000).

[47] T. Yoshida, M. Hashimoto, S. Ideta, A. Fujimori, K. Tanaka, N. Mannella, Z. Hussain, Z.-X. Shen, M. Kubota, K. Ono, S. Komiya, Y. Ando, H. Eisaki, and S. Uchida, Phys. Rev. Lett. **103**, 037004 (2009).

[48] A. Hackl and M. Vojta, Phys. Rev. B **80**, 220514 (2009).

[49] A. Hackl, M. Vojta, and S. Sachdev, Phys. Rev. B **81**, 045102 (2010).

[50] R. Daou, O. Cyr-Choinière, F. Laliberté, D. LeBoeuf, N. Doiron-Leyraud, J.-Q. Yan, J.-S. Zhou, J. B. Goodenough, and L. Taillefer, Phys. Rev. B **79**, 180505 (2009).

[51] J. M. Tranquada, J. D. Axe, N. Ichikawa, A. R. Moodenbaugh, Y. Nakamura, and S. Uchida, Phys. Rev. Lett. **78**, 338 (1997).

[52] A. W. Hunt, P. M. Singer, A. F. Cederström, and T. Imai, Phys. Rev. B **64**, 134525 (2001).

[53] J. D. Axe and M. K. Crawford, J. Low Temp. Phys. **95**, 271 (1994).

[54] B. Keimer, N. Belk, R. J. Birgeneau, A. Cassanho, C. Y. Chen, M. Greven, M. A. Kastner, A. Aharony, Y. Endoh, R. W. Erwin, and G. Shirane, Phys. Rev. B **46**, 14034 (1992).

[55] C. Hess, E. M. Ahmed, U. Ammerahl, A. Revcolevschi, and B. Büchner, Eur. Phys. J. Spec. Top. **188**, 103 (2010).

[56] J. Fink, V. Soltwisch, J. Geck, E. Schierle, E. Weschke, and B. Büchner, Phys. Rev. B **83**, 092503 (2011).

[57] J. H. Brewer, E. J. Ansaldo, J. F. Carolan, A. C. D. Chaklader, W. N. Hardy, D. R. Harshman, M. E. Hayden, M. Ishikawa, N. Kaplan, R. Keitel, J. Kempton, R. F. Kiefl, W. J. Kossler, S. R. Kreitzman, A. Kulpa, Y. Kuno, G. M. Luke, H. Miyatake, K. Nagamine, Y. Nakazawa, N. Nishida, K. Nishiyama, S. Ohkuma, T. M. Riseman, G. Roehmer, P. Schleger, D. Shimada, C. E. Stronach, T. Takabatake, Y. J. Uemura, Y. Watanabe, D. L. Williams, T. Yamazaki, and B. Yang, Phys. Rev. Lett. **60**, 1073 (1988).

[58] M. Hücker, V. Kataev, J. Pommer, J. Harraß, A. Hosni, C. Pflitsch, R. Gross, and B. Büchner, Phys. Rev. B **59**, 725(R) (1999).

[59] A. Kaminski, S. Rosenkranz, H. M. Fretwell, M. R. Norman, M. Randeria, J. C. Campuzano, J.-M. Park, Z. Z. Li, and H. Raffy, Phys. Rev. B **73**, 174511 (2006).

[60] T. Yoshida, X. J. Zhou, K. Tanaka, W. L. Yang, Z. Hussain, Z.-X. Shen, A. Fujimori, S. Sahrakorpi, M. Lindroos, R. S. Markiewicz, A. Bansil, S. Komiya, Y. Ando, H. Eisaki, T. Kakeshita, and S. Uchida, Phys. Rev. B **74**, 224510 (2006).

[61] W. Wu, M. S. Scheurer, S. Chatterjee, S. Sachdev, A. Georges, and M. Ferrero, arXiv:1707.06602.

[62] H. Braganca, S. Sakai, M. C. O. Aguiar, and M. Civelli, arXiv:1708.02084.

[63] L. Nie, A. V. Maharaj, E. Fradkin, and S. A. Kivelson, Phys. Rev. B **96**, 085142 (2017).

[64] B. Khaykovich, S. Wakimoto, R. J. Birgeneau, M. A. Kastner, Y. S. Lee, P. Smeibidl, P. Vorderwisch, and K. Yamada, Phys. Rev. B **71**, 220508 (2005).

[65] J. Chang, C. Niedermayer, R. Gilardi, N. B. Christensen, H. M. Rønnow, D. F. McMorrow, M. Ay, J. Stahn, O. Sobolev, A. Hiess, S. Pailhes, C. Baines, N. Momono, M. Oda, M. Ido, and J. Mesot, Phys. Rev. B **78**, 104525 (2008).

[66] H. Kimura, M. Kofu, Y. Matsumoto, and K. Hirota, Phys. Rev. Lett. **91**, 067002 (2003).

[67] C. Panagopoulos, J. Tallon, B. Rainford, J. Cooper, C. Scott, and T. Xiang, Solid State Commun. **126**, 47 (2003), in Proceedings of the High-Tc Superconductivity Workshop.

[68] C. Panagopoulos, A. P. Petrovic, A. D. Hillier, J. L. Tallon, C. A. Scott, and B. D. Rainford, Phys. Rev. B **69**, 144510 (2004).

[69] M. Hücker, N. B. Christensen, A. T. Holmes, E. Blackburn, E. M. Forgan, R. Liang, D. A. Bonn, W. N. Hardy, O. Gutowski, M. v. Zimmermann, S. M. Hayden, and J. Chang, Phys. Rev. B **90**, 054514 (2014).

[70] S. Blanco-Canosa, A. Frano, E. Schierle, J. Porras, T. Loew, M. Minola, M. Bluschke, E. Weschke, B. Keimer, and M. Le Tacon, Phys. Rev. B **90**, 054513 (2014).

[71] D. LeBoeuf, N. Doiron-Leyraud, B. Vignolle, M. Sutherland, B. J. Ramshaw, J. Levallois, R. Daou, F. Laliberté, O. Cyr-Choinière, J. Chang, Y. J. Jo, L. Balicas, R. Liang, D. A. Bonn, W. N. Hardy, C. Proust, and L. Taillefer, Phys. Rev. B **83**, 054506 (2011).

[72] D. Haug, V. Hinkov, Y. Sidis, P. Bourges, N. B. Christensen, A. Ivanov, T. Keller, C. T. Lin, and B. Keimer, New J. Phys. **12**, 105006 (2010).

[73] Y. Ando, K. Segawa, S. Komiya, and A. N. Lavrov, Phys. Rev. Lett. **88**, 137005 (2002).

[74] O. Cyr-Choinière, G. Grissonnanche, S. Badoux, J. Day, D. A. Bonn, W. N. Hardy, R. Liang, N. Doiron-Leyraud, and L. Taillefer, Phys. Rev. B **92**, 224502 (2015).

[75] B. Fauqué, Y. Sidis, V. Hinkov, S. Pailhès, C. T. Lin, X. Chaud, and P. Bourges, Phys. Rev. Lett. **96**, 197001 (2006).

[76] Y. Sidis and P. Bourges, J. Phys.: Conf. Series **449**, 012012 (2013).

[77] L. Mangin-Thro, Y. Li, Y. Sidis, and P. Bourges, Phys. Rev. Lett. **118**, 097003 (2017).

[78] T. P. Croft, C. Lester, M. S. Senn, A. Bombardi, and S. M. Hayden, Phys. Rev. B **89**, 224513 (2014).

[79] N. B. Christensen, J. Chang, J. Larsen, M. Fujita, M. Oda, M. Ido, N. Momono, E. M. Forgan, A. T. Holmes, J. Mesot, M. Huecker, and M. v. Zimmermann, arXiv:1404.3192.

[80] S. Badoux, S. A. A. Afshar, B. Michon, A. Ouellet, S. Fortier, D. LeBoeuf, T. P. Croft, C. Lester, S. M. Hayden, H. Takagi, K. Yamada, D. Graf, N. Doiron-Leyraud, and L. Taillefer, Phys. Rev. X **6**, 021004 (2016).

[81] M. Kofu, S.-H. Lee, M. Fujita, H.-J. Kang, H. Eisaki, and K. Yamada, Phys. Rev. Lett. **102**, 047001 (2009).

[82] S. Wakimoto, G. Shirane, Y. Endoh, K. Hirota, S. Ueki, K. Yamada, R. J. Birgeneau, M. A. Kastner, Y. S. Lee, P. M. Gehring, and S. H. Lee, Phys. Rev. B **60**, 769(R) (1999).

[83] B. Lake, H. M. Ronnow, N. B. Christensen, G. Aeppli, K. Lefmann, D. F. McMorrow, P. Vorderwisch, P. Smeibidl, N. Mangkorntong, T. Sasagawa, M. Nohara, H. Takagi, and T. E. Mason, Nature (London) **415**, 299 (2002).

[84] H. Kimura, K. Hirota, H. Matsushita, K. Yamada, Y. Endoh, S.-H. Lee, C. F. Majkrzak, R. Erwin, G. Shirane, M. Greven, Y. S. Lee, M. A. Kastner, and R. J. Birgeneau, Phys. Rev. B **59**, 6517 (1999).

[85] V. Balédent, B. Fauqué, Y. Sidis, N. B. Christensen, S. Pailhès, K. Conder, E. Pomjakushina, J. Mesot, and P. Bourges, Phys. Rev. Lett. **105**, 027004 (2010).

[86] B. Nachumi, Y. Fudamoto, A. Keren, K. M. Kojima, M. Larkin, G. M. Luke, J. Merrin, O. Tchernyshyov, Y. J. Uemura, N. Ichikawa, M. Goto, H. Takagi, S. Uchida, M. K. Crawford, E. M. McCarron, D. E. MacLaughlin, and R. H. Heffner, Phys. Rev. B **58**, 8760 (1998).

[87] T. Wu, H. Mayaffre, S. Krämer, M. Horvatić, C. Berthier, P. L. Kuhns, A. P. Reyes, R. Liang, W. N. Hardy, D. A. Bonn, and M.-H. Julien, Nat. Commun. **4**, 2113 (2013).

[88] S. Blanco-Canosa, A. Frano, T. Loew, Y. Lu, J. Porras, G. Ghiringhelli, M. Minola, C. Mazzoli, L. Braicovich, E. Schierle, E. Weschke, M. Le Tacon, and B. Keimer, Phys. Rev. Lett. **110**, 187001 (2013).

[89] G. Grissonnanche, O. Cyr-Choinière, F. Laliberté, S. René de Cotret, A. Juneau-Fecteau, S. Dufour-Beauséjour, M.-E. Delage, D. LeBoeuf, J. Chang, B. J. Ramshaw, D. A. Bonn, W. N. Hardy, R. Liang, S. Adachi, N. E. Hussey, B. Vignolle, C. Proust, M. Sutherland, S. Kramer, J.-H. Park, D. Graf, N. Doiron-Leyraud, and L. Taillefer, Nat. Commun. **5**, 3280 (2014).

[90] J. Chang, M. Shi, S. Pailhés, M. Månsson, T. Claesson, O. Tjernberg, A. Bendounan, Y. Sassa, L. Patthey, N. Momono, M. Oda, M. Ido, S. Guerrero, C. Mudry, and J. Mesot, Phys. Rev. B **78**, 205103 (2008).

[91] F. Laliberté, J. Chang, N. Doiron-Leyraud, E. Hassinger, R. Daou, M. Rondeau, B. Ramshaw, R. Liang, D. Bonn, W. Hardy, S. Pyon, T. Takayama, H. Takagi, I. Sheikin, L. Malone, C. Proust, K. Behnia, and L. Taillefer, Nat. Commun. **2**, 432 (2011).

[92] J. M. Tranquada, B. J. Sternlieb, J. D. Axe, Y. Nakamura, and S. Uchida, Nature (London) **375**, 561 (1995).

[93] J. E. Hoffman, E. W. Hudson, K. M. Lang, V. Madhavan, H. Eisaki, S. Uchida, and J. C. Davis, Science **295**, 466 (2002).

[94] C. Howald, H. Eisaki, N. Kaneko, and A. Kapitulnik, Proc. Natl. Acad. Sci. USA **100**, 9705 (2003).

[95] N. Doiron-Leyraud, C. Proust, D. LeBoeuf, J. Levallois, J.-B. Bonnemaison, R. Liang, D. A. Bonn, W. N. Hardy, and L. Taillefer, Nature (London) **447**, 565 (2007).

[96] D. LeBoeuf, N. Doiron-Leyraud, J. Levallois, R. Daou, J.-B. Bonnemaison, N. E. Hussey, L. Balicas, B. J. Ramshaw, R. Liang, D. A. Bonn, W. N. Hardy, S. Adachi, C. Proust, and L. Taillefer, Nature (London) **450**, 533 (2007).

[97] L. Taillefer, J. Phys.: Condens. Matter **21**, 164212 (2009).

[98] J. Chang, R. Daou, C. Proust, D. LeBoeuf, N. Doiron-Leyraud, F. Laliberté, B. Pingault, B. J. Ramshaw, R. Liang, D. A. Bonn, W. N. Hardy, H. Takagi, A. B. Antunes, I. Sheikin, K. Behnia, and L. Taillefer, Phys. Rev. Lett. **104**, 057005 (2010).

[99] T. Wu, H. Mayaffre, S. Krämer, M. Horvatić, C. Berthier, W. N. Hardy, R. Liang, D. A. Bonn, and M.-H. Julien, Nature (London) **477**, 191 (2011).

[100] G. Ghiringhelli, M. Le Tacon, M. Minola, S. Blanco-Canosa, C. Mazzoli, N. B. Brookes, G. M. De Luca, A. Frano, D. G. Hawthorn, F. He, T. Loew, M. M. Sala, D. C. Peets, M. Salluzzo, E. Schierle, R. Sutarto, G. A. Sawatzky, E. Weschke, B. Keimer, and L. Braicovich, Science **337**, 821 (2012).

[101] J. Chang, E. Blackburn, A. T. Holmes, N. B. Christensen, J. Larsen, J. Mesot, R. Liang, D. A. Bonn, W. N. Hardy, A. Watenphul, M. v. Zimmermann, E. M. Forgan, and S. M. Hayden, Nat. Phys. **8**, 871 (2012).

[102] M. v. Zimmermann, A. Vigliante, T. Niemöller, N. Ichikawa, T. Frello, J. Madsen, P. Wochner, S. Uchida, N. H. Andersen, J. M. Tranquada, D. Gibbs, and J. R. Schneider, Europhys. Lett. **41**, 629 (1998).

[103] T. Niemöller, N. Ichikawa, T. Frello, H. Hünnefeld, N. H. Andersen, S. Uchida, J. R. Schneider, and J. M. Tranquada, Eur. Phys. J. B **12**, 509 (1999).
[104] J. Fink, E. Schierle, E. Weschke, J. Geck, D. Hawthorn, V. Soltwisch, H. Wadati, H.-H. Wu, H. A. Dürr, N. Wizent, B. Büchner, and G. A. Sawatzky, Phys. Rev. B **79**, 100502 (2009).
[105] W. Tabis, Y. Li, M. L. Tacon, L. Braicovich, A. Kreyssig, M. Minola, G. Dellea, E. Weschke, M. J. Veit, M. Ramazanoglu, A. I. Goldman, T. Schmitt, G. Ghiringhelli, N. Barišić, M. K. Chan, C. J. Dorow, G. Yu, X. Zhao, B. Keimer, and M. Greven, Nat. Commun. **5**, 5875 (2014).
[106] E. H. da Silva Neto, P. Aynajian, A. Frano, R. Comin, E. Schierle, E. Weschke, A. Gyenis, J. Wen, J. Schneeloch, Z. Xu, S. Ono, G. Gu, M. Le Tacon, and A. Yazdani, Science **343**, 393 (2014).
[107] R. Comin, A. Frano, M. M. Yee, Y. Yoshida, H. Eisaki, E. Schierle, E. Weschke, R. Sutarto, F. He, A. Soumyanarayanan, Y. He, M. Le Tacon, I. S. Elfimov, J. E. Hoffman, G. A. Sawatzky, B. Keimer, and A. Damascelli, Science **343**, 390 (2014).
[108] M. Schütt and R. M. Fernandes, Phys. Rev. Lett. **115**, 027005 (2015).
[109] S. Okamoto, D. Sénéchal, M. Civelli, and A.-M. S. Tremblay, Phys. Rev. B **82**, 180511 (2010).
[110] A. F. Bangura, P. M. C. Rourke, T. M. Benseman, M. Matusiak, J. R. Cooper, N. E. Hussey, and A. Carrington, Phys. Rev. B **82**, 140501 (2010).
[111] T. Kondo, T. Takeuchi, T. Yokoya, S. Tsuda, S. Shin, and U. Mizutani, J. Electron Spectrosc. Relat. Phenom. **137–140**, 663 (2004), iCESS-9 Proceedings of the 9th International Conference on Electronic Spectroscopy and Structure.
[112] B. Vignolle, A. Carrington, R. A. Cooper, M. M. J. French, A. P. Mackenzie, C. Jaudet, D. Vignolles, C. Proust, and N. E. Hussey, Nature (London) **455**, 952 (2008).
[113] T. Manako, Y. Kubo, and Y. Shimakawa, Phys. Rev. B **46**, 11019 (1992).
[114] A. P. Mackenzie, S. R. Julian, D. C. Sinclair, and C. T. Lin, Phys. Rev. B **53**, 5848 (1996).
[115] C. Proust, E. Boaknin, R. W. Hill, L. Taillefer, and A. P. Mackenzie, Phys. Rev. Lett. **89**, 147003 (2002).
[116] S. Nakamae, K. Behnia, N. Mangkorntong, M. Nohara, H. Takagi, S. J. C. Yates, and N. E. Hussey, Phys. Rev. B **68**, 100502 (2003).
[117] M. Abdel-Jawad, J. G. Analytis, L. Balicas, A. Carrington, J. P. H. Charmant, M. M. J. French, and N. E. Hussey, Phys. Rev. Lett. **99**, 107002 (2007).
[118] L. Taillefer, Annu. Rev. Condens. Matter Phys. **1**, 51 (2010).
[119] N. Doiron-Leyraud, P. Auban-Senzier, S. René de Cotret, C. Bourbonnais, D. Jérome, K. Bechgaard, and L. Taillefer, Phys. Rev. B **80**, 214531 (2009).
[120] F. F. Tafti, F. Laliberté, M. Dion, J. Gaudet, P. Fournier, and L. Taillefer, Phys. Rev. B **90**, 024519 (2014).
[121] I. Ussishkin, S. L. Sondhi, and D. A. Huse, Phys. Rev. Lett. **89**, 287001 (2002).
[122] M. N. Serbyn, M. A. Skvortsov, A. A. Varlamov, and V. Galitski, Phys. Rev. Lett. **102**, 067001 (2009).
[123] K. Michaeli and A. M. Finkel'stein, Europhys. Lett. **86**, 27007 (2009).
[124] V. J. Emery and S. A. Kivelson, Nature (London) **374**, 434 (1995).
[125] Y. Dagan, M. M. Qazilbash, C. P. Hill, V. N. Kulkarni, and R. L. Greene, Phys. Rev. Lett. **92**, 167001 (2004).
[126] A. Pourret, H. Aubin, J. Lesueur, C. A. Marrache-Kikuchi, L. Berge, L. Dumoulin, and K. Behnia, Nat. Phys. **2**, 683 (2006).
[127] T. J. Reber, N. C. Plumb, Y. Cao, Z. Sun, Q. Wang, K. McElroy, H. Iwasawa, M. Arita, J. S. Wen, Z. J. Xu, G. Gu, Y. Yoshida, H. Eisaki, Y. Aiura, and D. S. Dessau, Phys. Rev. B **87**, 060506 (2013).
[128] T. Kondo, W. Malaeb, Y. Ishida, T. Sasagawa, H. Sakamoto, T. Takeuchi, T. Tohyama, and S. Shin, Nat. Commun. **6**, 7699 (2015).
[129] J. Lee, K. Fujita, A. R. Schmidt, C. K. Kim, H. Eisaki, S. Uchida, and J. C. Davis, Science **325**, 1099 (2009).
[130] K. K. Gomes, A. N. Pasupathy, A. Pushp, S. Ono, Y. Ando, and A. Yazdani, Nature (London) **447**, 569 (2007).
[131] Y. Okada, Y. Kuzuya, T. Kawaguchi, and H. Ikuta, Phys. Rev. B **81**, 214520 (2010).
[132] G. Yu, D.-D. Xia, N. Barišić, R.-H. He, N. Kaneko, T. Sasagawa, Y. Li, X. Zhao, A. Shekhter, and M. Greven, arXiv:1210.6942.
[133] G. Yu, D.-D. Xia, D. Pelc, R.-H. He, N. Kaneko, T. Sasagawa, Y. Li, X. Zhao, N. Barišić, A. Shekhter, and M. Greven, arXiv:1710.10957.
[134] J. Corson, R. Mallozzi, J. Orenstein, J. N. Eckstein, and I. Bozovic, Nature (London) **398**, 221 (1999).
[135] M. S. Grbić, M. Požek, D. Paar, V. Hinkov, M. Raichle, D. Haug, B. Keimer, N. Barišić, and A. Dulčić, Phys. Rev. B **83**, 144508 (2011).
[136] W. S. Lee, I. M. Vishik, K. Tanaka, D. H. Lu, T. Sasagawa, N. Nagaosa, T. P. Devereaux, Z. Hussain, and Z. X. Shen, Nature (London) **450**, 81 (2007).
[137] L. S. Bilbro, R. V. Aguilar, G. Logvenov, O. Pelleg, I. Božovi'c, and N. P. Armitage, Nat. Phys. **7**, 298 (2011).
[138] Y. Wang, N. P. Ong, Z. A. Xu, T. Kakeshita, S. Uchida, D. A. Bonn, R. Liang, and W. N. Hardy, Phys. Rev. Lett. **88**, 257003 (2002).
[139] Y. Wang, S. Ono, Y. Onose, G. Gu, Y. Ando, Y. Tokura, S. Uchida, and N. P. Ong, Science **299**, 86 (2003).
[140] L. Li, Y. Wang, S. Komiya, S. Ono, Y. Ando, G. D. Gu, and N. P. Ong, Phys. Rev. B **81**, 054510 (2010).
[141] J. F. Yu, B. J. Ramshaw, I. Kokanović, K. A. Modic, N. Harrison, J. Day, R. Liang, W. N. Hardy, D. A. Bonn, A. McCollam, S. R. Julian, and J. R. Cooper, Phys. Rev. B **92**, 180509 (2015).
[142] R. I. Rey, A. Ramos-Álvarez, J. Mosqueira, M. V. Ramallo, and F. Vidal, Phys. Rev. B **87**, 056501 (2013).
[143] I. Kokanović, D. J. Hills, M. L. Sutherland, R. Liang, and J. R. Cooper, Phys. Rev. B **88**, 060505 (2013).